REVIEW ARTICLE | MAY 28 2026

Vibrational exciton nano-spectroscopy: Probing molecular order and disorder on the nanoscale

Richard L. Puro ; Markus B. Raschke

Chem. Phys. Rev. 7, 021309 (2026)
https://doi.org/10.1063/5.0310896

Chemical Physics Reviews REVIEW pubs.aip.org/aip/cpr

Vibrational exciton nano-spectroscopy: Probing molecular order and disorder on the nanoscale

Cite as: Chem. Phys. Rev. **7**, 021309 (2026); doi: 10.1063/5.0310896
Submitted: 5 November 2025 · Accepted: 11 May 2026 ·
Published Online: 28 May 2026

View Online Export Citation CrossMark

Richard L. Puro[a] and Markus B. Raschke[b]

AFFILIATIONS

Department of Physics, University of Colorado, Boulder, Colorado 80309, USA

[a]Electronic mail: richard.puro@colorado.edu
[b]Author to whom correspondence should be addressed: markus.raschke@colorado.edu

ABSTRACT

Transition dipole coupling between localized molecular vibrations represents a fundamental mechanism of energy delocalization in molecular solids. These collective states, referred to as vibrational excitons, give rise to distinct vibrational frequency shifts and mode splitting encoding information about molecular orientation, packing, conformation, and structural disorder. Originally developed to describe ideal crystalline materials, vibrational exciton spectroscopy and modeling have since evolved into a versatile tool applicable to a broad range of chemical systems, including molecular crystals, self-assembled monolayers (SAMs), molecular liquids, and biomolecular assemblies. However, diffraction-limited vibrational Raman and IR spectroscopy spatially averages over macroscopic ensembles of molecules, making it challenging to resolve inhomogeneities on nanometer length scales, which dictate the overall response of many molecular solids. Recently extended to the nanoscale, vibrational coupling nano-crystallography (VCNC) combines IR scattering-type scanning near-field optical microscopy (IR *s*-SNOM) with vibrational exciton theory to spatially resolve local molecular order and domain structure with nanometer resolution. In this review, we describe recent advances in near-field spectroscopy of vibrational excitons to image local molecular order in crystals, SAMs, and biological systems. Finally, we conclude with a perspective for VCNC to study excited-state dynamics, energy transport, collective quantum phenomena, and nanoscale structural evolution in complex molecular systems.

TABLE OF CONTENTS

I. INTRODUCTION

Molecular solids are a broad class of materials in which molecules interact through weak intermolecular forces, such as London dispersion forces, hydrogen bonding, and dipole–dipole coupling.[1] Despite weak interactions compared to covalent or ionic bonding, a wide range of physical behaviors emerge, including electron or ion conductivity and optical properties.[2–4] The functional behavior of the solid thus derives not only from the behavior of its individual molecules, but also from the intermolecular coupling and associated macroscopic structure of the solid from amorphous to highly crystalline. The resulting structural versatility and tunable properties form the basis for applications in pharmaceuticals,[5] organic electronics,[6,7] energy conversion and storage,[8–10] and biological systems. A common feature of these systems is that their macroscopic functionality often arises from the nanoscale structural organization, which controls intermolecular interactions and charge and energy transport.[3,4,11–13]

Better elucidating the relationships between structure and functionality is essential for the rational design of materials with targeted and multifunctional properties. However, because of the low-energy scale of the intermolecular interactions with their soft potential and thus fragile (often dynamic) local molecular environment, few techniques can directly access the energy landscape of intermolecular coupling.

Vibrational solvatochromism in the form of environment-dependent Stark shifts has been well established to detect heterogeneity in local molecular environments, but is mainly applicable to amorphous molecular systems where vibrational modes can be described as localized oscillators.[14,15] In densely packed molecular solids, vibrational modes interact through transition dipole coupling, leading to a hybridization of the vibrational wavefunctions and collective delocalized excitations known as *vibrational excitons* (VEs), wherein the vibrational wavefunction spans across multiple neighboring molecules.[16–18] Even in amorphous liquids, vibrational wavefunctions have been shown to extend over more than 100 molecules in some model systems.[19] Such VE formation gives rise to characteristic broadening, frequency shifts, and mode splittings in vibrational spectra. However, these spectral features may easily be misattributed to molecular decomposition, chemical reactions, vibrational Stark shifts, or compositional heterogeneity.

The sensitivity of the vibrational spectrum to molecular orientation, packing, conformation, and short- to long-range order makes VE spectroscopy in principle a powerful structural probe. In particular, infrared (IR) spectroscopy enables the detection of crystallinity and structural transitions in, e.g., bulk solids, thin films, or molecular monolayers. Applications have included remote sensing of atmospheric aerosols,[20] monitoring self-assembly,[21,22] and characterizing protein secondary structure.[23,24] Additional insight into the dynamics of molecular solids has been achieved through multi-dimensional coherent IR spectroscopy (2D IR) to distinguish homogeneous and inhomogeneous broadening, probe ultrafast vibrational coupling, and reaction dynamics.[25]

However, many molecular materials are often spatially heterogeneous even when composed of a single molecular species due to phase segregation, domain formation, defects, and varying degrees of local crystallinity. Probing in the far-field even with diffraction-limited spatial resolution of $\sim\lambda/2$ then typically still averages over many degrees of structural heterogeneities, obfuscating the VE response. As a nanoscopic phenomenon, only by probing vibrational coupling at the length scale of the coupling interaction itself (few nanometers) can the local material morphology be deconvolved from effects due to long-range heterogeneity. Conventional ensemble-averaging techniques cannot distinguish broadening arising from structural disorder on nanometer length scales from gradual structural variations across hundreds of nanometers to micrometers. Recent advances in infrared near-field microscopy have enabled VEs to be probed at the nanoscale, allowing for the utilization of VEs as a nanoscopic tool to determine local order, disorder, crystallinity, and their kinetics on the length scales over which the vibrational wavefunction delocalizes.

Specifically, IR scattering-type scanning near-field optical microscopy (IR *s*-SNOM) has enabled spatially resolved vibrational imaging with nanometer resolution.[26–28] By adapting VE models to interpret local frequency shifts, IR *s*-SNOM provides unprecedented insight into nanoscale order, disorder, and coupling in molecular materials[29] (Fig. 1). This ability to map structural heterogeneity complements electron and x-ray diffraction and imaging techniques,

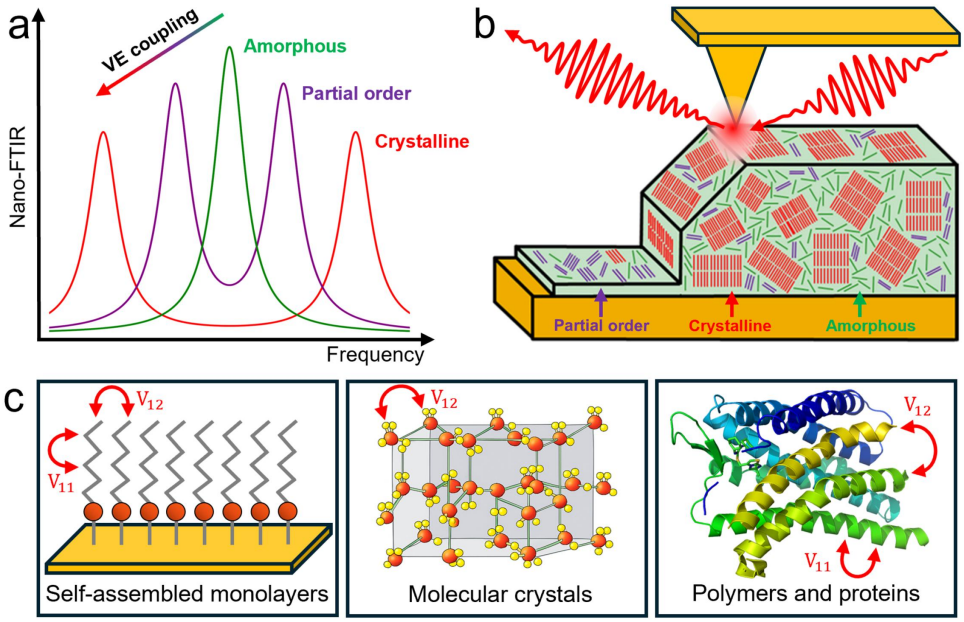

FIG. 1. Vibrational coupling nano-crystallography (VCNC) to study order and disorder in molecular solids based on peak splitting and spectral shifts to vibrational resonances induced by transition dipole coupling V_{ij}. A progressive peak splitting of the vibrational spectrum with increasing degree of molecular order is used for illustration, but details depend on the specific molecular arrangement within the crystal. (a) Spatio-spectral infrared vibrational nano-spectroscopy based on IR *s*-SNOM to determine crystallinity and intermolecular coupling with nanometer spatial resolution (b). VCNC is applicable to study self-assembled monolayers, molecular crystals, polymers, hybrid materials, and protein complexes among others (c).

which are primarily sensitive to long-range crystalline order rather than local molecular disorder.[30]

In this review, we discuss the theory and application of VEs in molecular solids and their role as a molecular ruler in the developing field of IR nano-spectroscopy. We survey experimental systems in which VE formation has been observed, discuss theoretical models used to describe the underlying intermolecular interactions, and highlight recent progress in applying these concepts to interpret nano-localized IR spectra in molecular crystals and related systems.

II. VIBRATIONAL EXCITON MODELING

The foundational theory of VEs was established by the example of molecular crystals, where transition dipole coupling (TDC) between vibrational modes approximated as localized oscillators was applied to model infrared vibrational spectra.[16–18,31–33] Early efforts focused on analytically tractable crystal structures such as crystalline benzene[34] and ethylene[33] using symmetry arguments to simplify the interaction Hamiltonian. However, due to the high computational demand to diagonalize large coupling matrices, progress stagnated until the widespread availability of modern computing resources. Today, a VE Hamiltonian can be numerically diagonalized for arbitrarily complex molecular systems without relying on symmetry simplifications, enabling accurate modeling of vibrational spectra in ordered molecular solids.

The following treatment of vibrational excitons closely follows the foundational derivation by Robert M. Hexter for crystalline solids[16] and later adapted by Peter Hamm and Martin T. Zanni for time-resolved spectroscopy.[25] In molecular solids, VEs arise from pairwise through-space coupling between vibrational modes approximated as local oscillators.[35] The VE is described by a tight-binding-like Hamiltonian

$$\hat{H} = \sum_{i=1}^{N} h\nu_i, b_i^\dagger b_i + \sum_{i<j} V_{ij}(b_i^\dagger b_j + b_j^\dagger b_i), \tag{1}$$

with ν_i the frequency of the local mode and $b_i^\dagger$ and b_i bosonic ladder operators for creation or annihilation of a vibrational quantum at site i. The coupling term V_{ij} arises from the bilinear part of a Taylor expansion of the intermolecular potential energy surface

$$V(q_1, \ldots, q_N) \approx \sum_{i=1}^{N} \frac{1}{2} V_{ii} q_i^2 + \sum_{i<j} 2V_{ij} q_i q_j, \tag{2}$$

with q_i the normal coordinate of vibration i expressed in terms of ladder operators,

$$q_i = \frac{1}{\sqrt{2}}(b_i^\dagger + b_i), \tag{3}$$

resulting in

$$q_i q_j = \frac{1}{2}(b_i^\dagger b_j + b_j^\dagger b_i + b_i b_j + b_i^\dagger b_j^\dagger). \tag{4}$$

The terms that change the number of vibrational quanta are neglected since the coupling between far detuned modes (those with different quanta of excitation) is small compared to coupling between resonant modes.[25] Thus, V_{ij} mediates resonant excitation hopping between sites.

The Hamiltonian is expanded in a single-excitation site basis of the individual vibrational states $|\phi_{nj}\rangle$, with n the number of vibrational energy quanta on site j,

$$|i\rangle = \left(\prod_{j\neq i} |\phi_{0j}\rangle\right)|\phi_{1i}\rangle, \tag{5}$$

resulting in the matrix representation

$$H = \begin{pmatrix} h\nu_1 & V_{12} & \cdots & V_{1N} \\ V_{21} & h\nu_2 & \cdots & V_{2N} \\ \vdots & \vdots & \ddots & \vdots \\ V_{N1} & V_{N2} & \cdots & h\nu_N \end{pmatrix}. \tag{6}$$

Diagonalizing H provides the coupled-mode eigenstates $|\psi_n\rangle$ and their eigenenergies E_n.

To simulate how coupling modifies the IR spectrum from the originally uncoupled molecules, the transition dipole moments are calculated for each eigenstate. The total transition dipole operator is given by

$$\vec{\mu} = \sum_i \vec{\mu}_i, \tag{7}$$

with $\vec{\mu}_i$ the dipole operator at site i. Expanding the eigenstate as

$$|\psi_n\rangle = \sum_{i=1}^{N} c_{ni}|i\rangle, \tag{8}$$

the transition dipole associated with the $|0\rangle \rightarrow |\psi_n\rangle$ excitation becomes

$$\langle\vec{\mu}\rangle_n = \sum_{i=1}^{N} c_{ni}\langle\vec{\mu}_i\rangle. \tag{9}$$

Thus, the transition dipole vector of each VE state is a superposition of local mode dipoles, weighted by the eigenvector coefficients c_{ni}.

The coupling V_{ij} between molecular sites i and j is then modeled using the TDC approximation

$$V_{ij} = \frac{1}{4\pi\epsilon_0}\left(\frac{\vec{\mu}_i \cdot \vec{\mu}_j}{r_{ij}^3} - \frac{3(\vec{r}_{ij} \cdot \vec{\mu}_i)(\vec{r}_{ij} \cdot \vec{\mu}_j)}{r_{ij}^5}\right), \tag{10}$$

where $\vec{r}_{ij}$ is the displacement vector between dipoles and $\vec{\mu}_i$ are the local transition dipole vectors.

Defining a position for each dipole requires knowledge of the change in electron charge distribution upon excitation of the vibrational mode. For skeletal modes involving motion of the molecular backbone, higher-order multipoles would need to be considered. In contrast, vibrations of small functional groups such as a carbonyl group (see Sec. IV) involve predominantly the localized motion of few atoms. It is thus appropriate to treat the vibrational transitions of such probe vibrations as point dipoles, which is a valid approximation for intermolecular distances sufficiently large such that the monopole fields from the positive and negative charge centers cancel, leaving only a dipole field (r^{-3} intensity scaling). This is the case for

intermolecular distances larger than the bond length of e.g., the carbonyl functional group of ∼1.5 Å.

A. Vibrational spectra of a coupled dimer

The basic features of VE formation can be illustrated by the example of a molecular dimer, i.e., two coupled vibrational oscillators of defined relative orientation and position. In this system, two eigenstates emerge with energies $h\nu \pm V_{12}$, corresponding to symmetric and antisymmetric combinations of the local modes [see Fig. 2(a)]. The associated transition dipole moments are $\vec{\mu}_1 \pm \vec{\mu}_2$, and the observed IR intensities are proportional to $|\vec{\mu}_1 \pm \vec{\mu}_2|^2$.

Figure 2(a) illustrates how the spectral response of the dimer depends on its internal geometry. For parallel dipoles, the symmetric eigenmode $\vec{\mu}_1 + \vec{\mu}_2$ is optically active due to constructive interference, while the antisymmetric mode $\vec{\mu}_1 - \vec{\mu}_2$ is not dipole allowed. The relative orientation of the two dipoles determines whether the symmetric mode is blue-shifted ($V > 0$) or red-shifted ($V < 0$). For orthogonal dipoles, the coupling vanishes if one dipole is also orthogonal to the displacement vector, but a peak splitting is observed with both symmetric and antisymmetric modes optically active otherwise. These examples illustrate how the dimer geometry is encoded in the resulting IR spectrum, though not uniquely as certain distinct geometries can yield similar spectral features. While IR spectroscopy alone cannot unambiguously determine the molecular packing, it can distinguish between different candidate arrangements based on observed spectral shifts and mode splitting.

Polarized IR measurements can further constrain the structural assignments. As shown in Fig. 2(b), for the indicated dimer configuration, the two eigenmodes have orthogonal polarization. Probing along $\hat{x}$ selects the red-shifted mode while probing along $\hat{y}$ selects the blue-shifted mode. Polarization-resolved IR measurements can thus provide additional insight into the absolute orientation of the dimer relative to the probe polarization, while the spectral features themselves provide insight into the orientations of the molecules relative to each other.

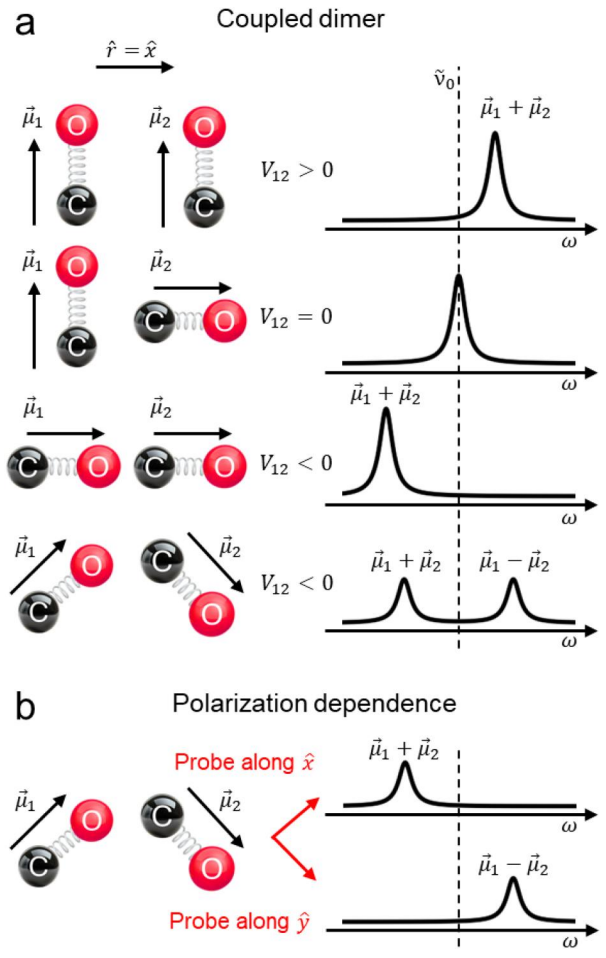

FIG. 2. Vibrational exciton modeling of a coupled molecular dimer. (a) Simulated spectra with different relative orientations exhibiting (from top to bottom) blue shift, no coupling, red shift, and peak splitting respectively. (b) Polarization dependence of a coupled spectrum illustrates how polarization-resolved measurements can identify the absolute orientation of the dimer pair.

B. Vibrational spectra of 2D molecular arrangement

The coupled dimer example illustrates how the VE spectrum depends on relative molecular orientation, but for molecular solids, the VE spectrum also depends on the number of molecules that participate in coupling. Extending exciton coupling to larger molecular assemblies, the VE spectrum is now calculated as a function of the delocalization length l_d of the vibrational wavefunction. We consider VEs in the two-dimensional arrangement indicated in Fig. 3(a) where the vibrational transition dipoles are oriented normal to the surface and form domains of varying size (number of molecules N) representing a molecular monolayer. The approach to modeling vibrational spectra as a function of l_d generalizes to 3D systems.

Figure 3(b) shows the VE states and their IR intensities for a square lattice of $N = 400$ molecules. Although 400 eigenmodes exist, only a small subset carry significant oscillator strength, leading to a sharp, collective IR-active absorption feature. The total spectrum (black curve) is constructed by summing Lorentzian lineshapes centered at each eigenenergy (dotted blue) with linewidth Γ equal to that of the isolated transition (in this example, $\Gamma = 5\,\mathrm{cm}^{-1}$). The calculated evolution of the VE resonance as a function of domain size N is shown in Fig. 3(c). With increasing domain size, the collective coupling increases, leading to a progressive blueshift, converging at $\Delta\tilde{\nu} \sim 13\,\mathrm{cm}^{-1}$ relative to the uncoupled mode. In contrast, the linewidth of the VE spectrum is largely independent of N [Fig. 3(a), lower].

This model was successfully employed to interpret nano-FTIR[36] and surface-enhanced Raman spectra[37] of p-nitrothiophenol (pNTP) self-assembled monolayers (SAMs) on gold, where variations in peak position were attributed to changes in domain size and chemical composition (see Sec. IV for details). The modeling assumed that the coupled spectra are independent of domain shape—an approximation that breaks down for particularly elongated or highly irregular geometries. Figure 4(a) demonstrates this effect for a fixed number of 64 molecules arranged in domains of different shape (2×32, 4×16, and 8×8), i.e., varying surface (circumference) to volume (area) ratio. Elongated domains exhibit reduced spectral shifts due to an effective

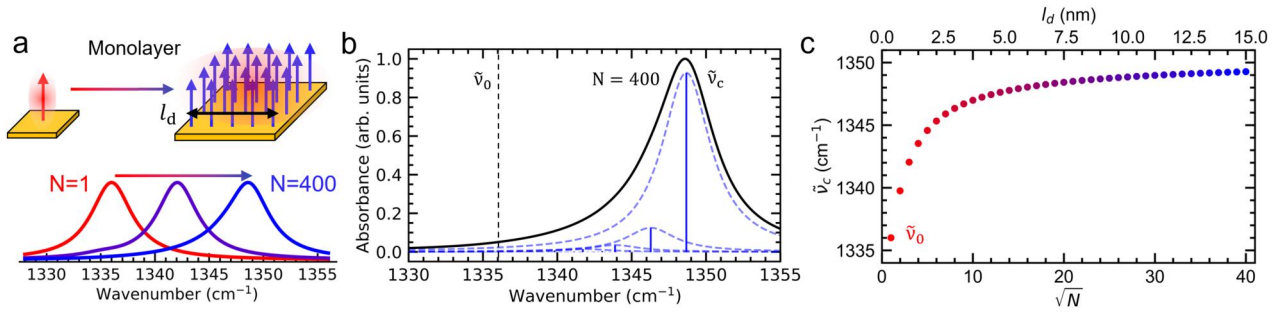

FIG. 3. Modeling of vibrational mode coupling for a molecular monolayer. (a) Schematic of a 2D parallel molecular arrangement of varying domain size ($N = 1 \ldots 400$). (b) Vibrational exciton mode distribution and corresponding intensities for a square of 20×20 molecules (blue vertical lines) with simulated spectrum overlaid (black), as the sum of absorption profiles for each mode with fixed FWHM of 5 cm^{-1} (blue, dotted). (c) Evolution of modeled center frequency (from Lorentzian fits to the simulated spectra) with increasing domain size.

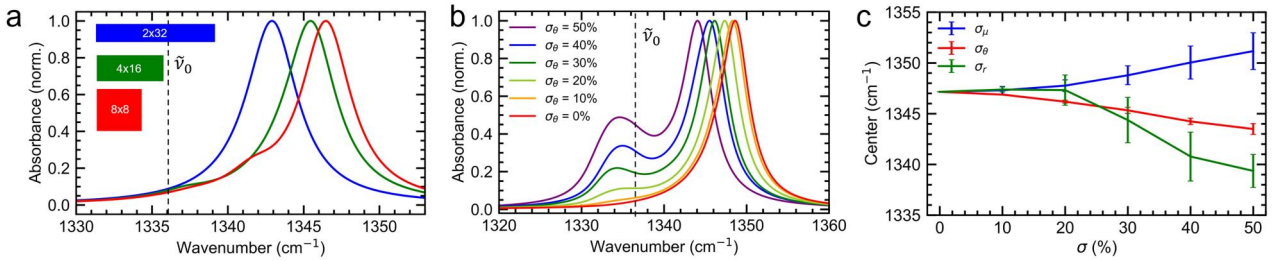

FIG. 4. Effects of domain geometry and molecular disorder on vibrational exciton spectra. (a) Modeled dependence of vibrational exciton spectra on domain shape for fixed number of molecules N. (b) Vibrational exciton spectra for square domains of 20×20 molecules with tilt angle noise of each molecule (θ and ϕ) based on a normal distribution with varying standard deviation σ_θ. (c) Modeled center frequency and uncertainty of the upper VE mode with σ ranging from 0% to 50% for transition dipole magnitude (σ_μ, blue), tilt angle (σ_θ, red), and position in the xy plane (σ_r, green).

increase in surface molecules with fewer neighbors and thus reduced collective coupling.

In addition, orientational disorder impacts the VE spectrum. Figure 4(b) shows how random angular disorder in molecular orientation reduces the blue shift and broadens the spectrum, with molecules on average oriented vertically but with tilt angle noise following a normal distribution with varying standard deviation σ_θ. The low-energy shoulder emerging for large degree of disorder corresponds to the in-plane component of the transition dipoles, which are distributed randomly and thus exhibit a slight broadening but a negligible systematic shift from $\tilde{\nu}_0$. Figure 4(c) shows the frequency of the coupled peak, derived from a Lorentzian fit to the $\tilde{\nu} > 1340$ cm^{-1} spectral region, and its variance across many trials as a function of disorder for different structural characteristics: transition dipole magnitude (σ_μ), orientation angle (σ_θ), and molecular position (σ_r). All sources of disorder produce similar trends, namely, shifts of <1 cm^{-1} for small values of σ, and large deviations beyond $\sigma > 20\%$. This shows how defects, disorder, and domain boundaries control the degree of coupling which manifests in the characteristics of the resulting VE spectrum.

III. VIBRATIONAL COUPLING NANO-CRYSTALLOGRAPHY (VCNC)

Conventional, ensemble-averaging far-field IR and Raman spectroscopy of VEs has been successfully applied to determine molecular packing and arrangement in molecular crystals,[20,35,38–42] self-assembled monolayers (SAMs),[22,43,44] and biological systems.[45–47] Nonlinear IR techniques provide additional insights such as multi-dimensional coherent IR spectroscopy (2D IR), which has been demonstrated to distinguish between homogeneous and inhomogeneous broadening and to probe ultrafast dynamics of intra- and intermolecular coupling and spectral diffusion, providing detailed insight into the local dynamical environment of VEs.[48–53] Sum-frequency generation spectroscopy (SFG), a second-order nonlinear technique, provides surface sensitivity. Probing only the top few molecular layers based on its electric-dipole selection rule, it can access vibrational excitons localized near interfaces.[54,55] Furthermore, it provides symmetry selectivity with respect to domain orientation, which can provide additional insight into surface ordering. However, these far-field, diffraction-limited techniques inherently average over macroscopic ensembles of molecules (in the lateral dimensions for SFG), obscuring spatial heterogeneity in the vibrational response. In particular, in molecular solids where domains may exhibit different intermolecular coupling strengths, disorder, or packing, ensemble measurements cannot resolve how VE coupling varies spatially within the material. Addressing this limitation requires spatially resolved probing of the local vibrational response at nanometer length scales.

Infrared scattering-type scanning near-field optical microscopy (IR *s*-SNOM), in its broadband infrared nano-spectroscopy application (nano-FTIR), can spatially resolve the local vibrational response

with deep sub-diffraction spatial resolution. Nano-FTIR enables direct visualization of spatial heterogeneities in VE coupling—for example, within crystalline grains, across domain boundaries, or identifying defects—revealing the nanoscopic spatial fabric of the material. Extending VE spectroscopy to the nanoscale resolves vibrational coupling on length scales comparable to its wavefunction delocalization.[14,29,56,57] Accessing these local, near-homogeneous sub-ensembles enables the intrinsic delocalization length of the vibrational wavefunction l_d to be determined and its spatial variation to be imaged over macroscopic distances, effectively using the VE itself as a molecular ruler for quantifying order in molecular materials.

A. Nano-FTIR spectroscopy

In the nano-FTIR (broadband) implementation of IR *s*-SNOM, mid-IR light is focused onto the metallic probe tip of an atomic force microscope (AFM) [Figs. 5(a) and 5(b)].[14,28,58] Common light sources for generating the necessary mid-IR radiation are femtosecond optical parametric oscillators (OPO) or amplifiers (OPA) combined with difference frequency generation (DFG), non-collinear OPA (NOPA) with DFG, and synchrotron IR radiation.[59] These light sources offer low noise and high spectral irradiance, which is ideal for resolving small VE frequency shifts in the nano-localized vibrational spectra. VE splittings rarely exceed 100 cm^{-1}, so typical OPO/OPA with DFG spectral bandwidths of ~200 cm^{-1} are sufficient for resolving relevant spectral features. Ultrabroadband NOPA with DFG or synchrotron IR radiation offers higher bandwidth, but lower spectral irradiance, which is beneficial for larger VE shifts or simultaneously resolving multiple vibrational resonances.

The tip-scattered IR light, composed of the near-field signal of interest E_{NF} and background scattering from the tip shaft and sample E_{BG}, is heterodyne amplified with a reference field E_R in an asymmetric Michelson interferometer [Fig. 5(a)]. The total signal intensity I detected by a mercury–cadmium–telluride (MCT) photodiode is given by

$$I(\tau) = |E_R(\tau) + E_{NF} + E_{BG}|^2, \tag{11}$$

expanding to

$$I(\tau) = |E_R(\tau)|^2 + |E_{NF}|^2 + |E_{BG}|^2 + 2\Re\left[E_{NF}E_R^*(\tau) + E_R(\tau)E_{BG}^* + E_{NF}E_{BG}^*\right], \tag{12}$$

with τ the delay of the reference pulse relative to the tip-scattered field.[60] To separate E_{NF} from E_{BG}, lock-in detection can be applied to detect the signal components at harmonics of the tip-tapping frequency $n\omega_t$. With background scattering mainly constant or linearly dependent on tip height over long range, but near-field scattering depending nonlinearly on tip height over short range, detecting harmonics with $n \geq 2$ separates E_{NF} from E_{BG}.[27,28] Lock-in detection thus isolates terms in Eq. (12) containing E_{NF}, leaving

$$I^{n\omega_t}(\tau) = 2\Re\left[E_{NF}^{n\omega_t}E_R^*(\tau) + E_{NF}^{n\omega_t}E_{BG}^*\right], \tag{13}$$

neglecting the term $|E_{NF}|^2$ since $E_R, E_{BG} \gg E_{NF}$. Varying τ, the resulting interferogram represents the cross-correlation between E_R and E_{NF} [Fig. 5(c)], while the background term $E_{NF}^{n\omega_t}E_{BG}^*$ appears only as a constant offset independent of τ. The Fourier transform then provides the spectral amplitude and phase of E_{NF},

$$\mathcal{F}\{I^{n\omega_t}\}(\nu) \propto E_{NF}^{n\omega_t}(\nu) = E_{0,n}(\nu)e^{i\phi_n(\nu)}, \tag{14}$$

where $\phi_n(\nu)$ is the near-field phase relative to the reference field. Normalizing the sample near-field spectra to a reference with a spectrally flat response (e.g., Au or doped Si) provides the desired phase and amplitude response of the sample.

The real and imaginary components $\Re[E_{NF}](\nu)$ and $\Im[E_{NF}](\nu)$, or similarly for small phase responses the amplitude $E_{0,n}(\nu)$ and phase $\phi_n(\nu)$, relate to the sample dispersion n and absorption coefficient κ, respectively, defined by the material dielectric function ε_r as $\sqrt{\varepsilon_r} = n + i\kappa$ [Fig. 5(d)].[28] Nano-FTIR spectra are commonly represented in both coordinate systems in the literature, with the Cartesian representation often preferred when the phase response is large, while the polar representation is often preferred when the phase response is small as $\phi_n(\nu)$ is a normalized quantity not dependent on incident field amplitude offering easier comparison between measurements. Resonances in the measured near-field spectra can be modeled as Lorentzian or Voigt profiles to extract the center frequency ν_0, linewidth Γ, and relative amplitude A of vibrational resonance features. For samples with weak localized resonances like molecular vibrations, extrinsic tip-sample interactions can cause small shifts in ν_0 compared to the intrinsic sample response, which can be corrected through

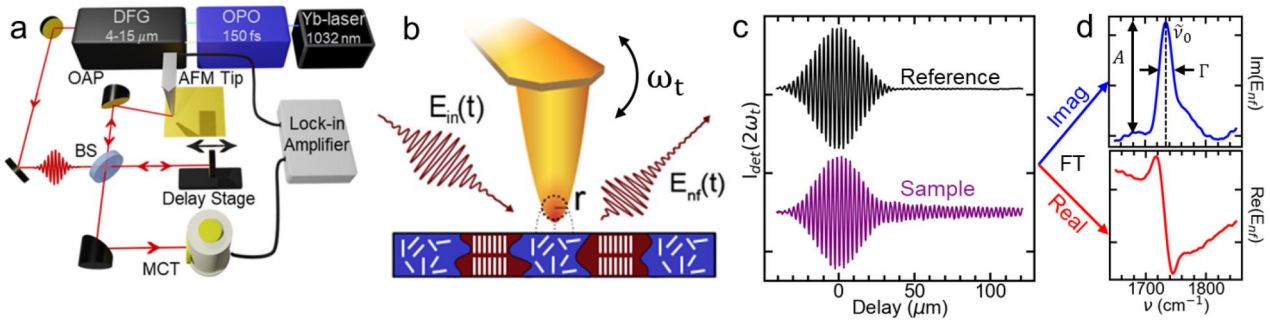

FIG. 5. Near-field vibrational IR spectroscopy. (a) Experimental setup for infrared scanning–scattering near-field optical microscopy (IR *s*-SNOM) with interferometry for signal detection. (b) Nano-FTIR imaging of heterogeneous environments with *s*-SNOM probe tip. (c) Representative interferograms measured on non-resonant reference (Au film, black) and resonant sample material (PMMA film with carbonyl resonance, purple). (d) Corresponding Fourier-transformed referenced carbonyl vibrational near-field spectra with imaginary (blue) and real (red) components.

modeling the probe tip as a polarizable point dipole (point dipole model),[61] an extended dipole (finite dipole model),[62] or more refined numerical approaches.[63] When determining relative frequency shifts between two resonances, such modeling procedures are important if the amplitude of the two features is different, as tip-sample interactions may affect the two resonances differently. If resonances are very weak, such as peaks in $\phi_n(\nu)$ below 0.1 radians often observed in molecular monolayers, or the difference in frequency between two resonances of comparable amplitude is desired, fitting nano-FTIR spectra without a model of tip-sample interaction can be sufficient.

B. Vibrational coupling nano-crystallography

IR *s*-SNOM was first applied to study vibrational coupling in molecular crystals at the example of the metalloporphyrin complex octaethyl–porphine ruthenium(II)carbonyl (RuOEP) dispersed in poly(3-hexylthiophene) (P3HT)[29] [Fig. 6(a)]. An evolution of the carbonyl spectrum from a single resonance ($\tilde{\nu}_0$) to two resonances ($\tilde{\nu}_+$ and $\tilde{\nu}_-$) is observed during crystallization in ensemble-averaging far-field FTIR [Fig. 6(b)]. The coexistence of the two VE features $\tilde{\nu}_+$ and $\tilde{\nu}_-$ upon crystallization was previously interpreted as molecules within crystals experiencing different local environments. It was hypothesized that RuOEP molecules would form 1D chains in which the interior carbonyl groups would experience a red shift while the capping carbonyls would experience a blue shift.[64] However, VE modeling and VCNC probing of the carbonyl mode in the RuOEP crystal structure subsequently demonstrated that the two $\tilde{\nu}_+$ and $\tilde{\nu}_-$ resonances are in fact a vibrationally coupled peak splitting and their spatial variation a measure of the degree of crystallinity within the three dimensional crystal structure of RuOEP.

Moreover, IR *s*-SNOM measurements of the RuOEP crystals revealed an additional resonance at the uncoupled $\tilde{\nu}_0$ frequency [Fig. 6(d)], indicating the coexistence of ordered and disordered regions even on nanometer length scales.[29] This $\tilde{\nu}_0$ feature, observed even in highly crystalline samples, was initially attributed to a subpopulation of fully amorphous molecules phase-separated from the crystalline domains. However, an amorphous domain would be expected to exhibit a significantly broadened $\tilde{\nu}_0$ resonance, similar to the initial FTIR spectrum before solvent annealing in Fig. 6(b), which is not observed. A more consistent explanation is that the $\tilde{\nu}_0$ resonance arises from slight orientational disorder within otherwise ordered domains, analogous to the mode shown in the model calculation in Fig. 4(b). Small deviations in molecular orientation introduce components of the transition dipole moment that are perpendicular to the primary coupling axis or plane. Because dipole components along this perpendicular direction are disordered, these components remain effectively uncoupled. As a result, individual molecules can simultaneously contribute to both the collective (coupled) VE response and a residual $\tilde{\nu}_0$ resonance,

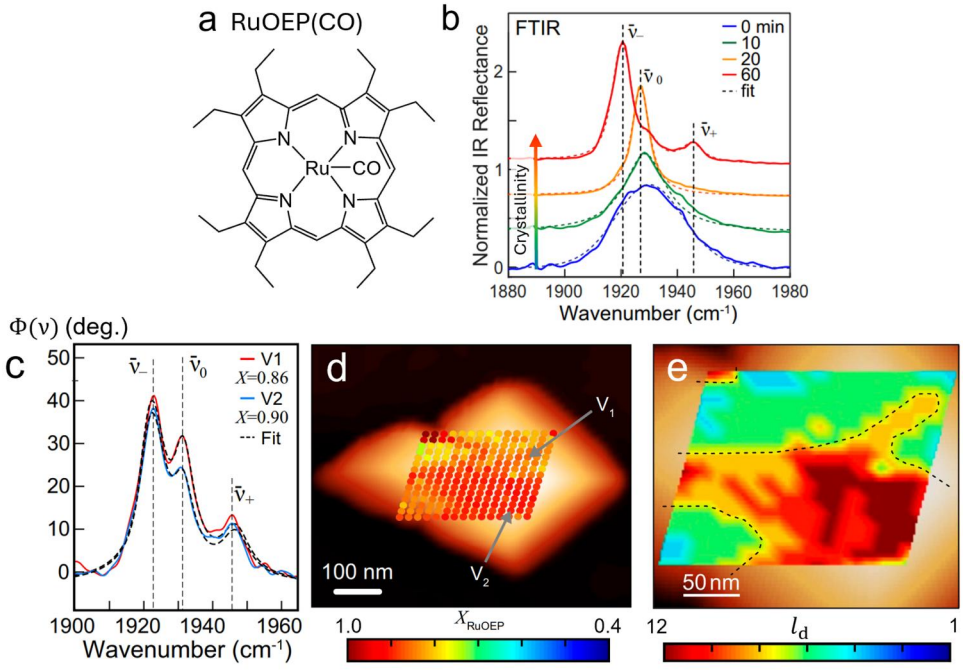

FIG. 6. Crystallinity and vibrational wavefunction delocalization derived from nano-FTIR spatio-spectral imaging. (a) Molecular structure of octaethyl-porphine ruthenium(II)carbonyl (RuOEP) and (b) carbonyl vibrational spectrum upon crystallization measured in micro-FTIR spectroscopy. RuOEP crystals are grown through solvent annealing evolving from amorphous RuOEP mixed in P3HT (blue) to crystalline RuOEP clusters (red) exhibiting VE splitting. (c) Nano-IR vibrational spectra measured on crystals of RuOEP containing three features corresponding to residual molecules in an amorphous phase ($\tilde{\nu}_0$) and molecules in a crystalline phase exhibiting VE coupling ($\tilde{\nu}_\pm$). (d) Nano-localized crystallinity calculated as the percentage of molecules in a crystalline phase. (e) Nano-localized VE delocalization length l_d calculated by comparing the center frequency of VE absorption features to VE modeling. Adapted with permission form Muller *et al.*, Proc. Natl. Acad. Sci. U. S. A. **117**, 7030–7037 (2020). Copyright 2020 Authors, licensed under CC BY 4.0.[29]

rather than existing as entirely coupled or entirely uncoupled species.

The coexistence of a VE response and $\tilde{\nu}_0$ response enabled quantifying the degree of local molecular order in two distinct ways. Fitting the vibrational spectra with a three Lorentzian model and applying the point dipole approximation to account for tip-sample interactions, the center frequency, linewidth, and amplitude of each resonance are determined with wavenumber resolution. Local crystallinity χ_{RuOEP} is then determined as the fraction of molecules in a coupled state based on the peak area $\Phi \propto A \cdot \Gamma$ of each resonance [Fig. 6(c)] with

$$\chi_{\mathrm{RuOEP}} \approx \Phi(\tilde{\nu}_-)/[\Phi(\tilde{\nu}_-) + \Phi(\tilde{\nu}_0)], \tag{15}$$

where Φ represents the area of each spectral peak and $\Phi(\tilde{\nu}_-)$ is used to represent the VE absorption because it contains a majority of the VE oscillator strength.

Alternatively, VE modeling is applied to relate the correlated variations in center frequencies of $\tilde{\nu}_-$ and $\tilde{\nu}_+$ to l_d [defined as the domain size for which VE modeling reproduces the measured vibrational spectrum, Fig. 6(e)]. Long delocalization is attributed to a high degree of crystalline order. Crystallinity, as defined here, describes the fraction of molecules in a coupled state, while l_d describes the distance over which vibrations interact. Crystallinity and l_d are different metrics for molecular order and are not trivially related, but it was shown the two correlate well [Figs. 6(d) and 6(e)], implying that l_d is a useful measure of structural order in molecular crystals.[29]

Following this initial demonstration, interpreting IR *s*-SNOM spectra in terms of VE coupling has been utilized in a range of materials including crystalline solids,[56] monolayers,[36,37] and polymers.[57,65] However, these studies did not precharacterize $\vec{\mu}_i$ and $\vec{r}_{ij}$, deriving these values in part based on fits to measured spectra. With the transition dipole magnitude or molecular positions and orientations left as fit parameters, l_d could not be determined quantitatively and rather l_d at different locations was compared qualitatively. A framework for quantitative VCNC was recently proposed in which l_d is the only free parameter by precharacterizing $\vec{\mu}_i$ and $\vec{r}_{ij}$. Its predictive accuracy was validated at the example of an RuOEP derivative functionalized with 5,5-dimethyl-1-pyrroline N-oxide (RuOEP-DMPO),[56] chosen because of its known crystal structure and strong carbonyl vibrational resonance.

For a given molecule of interest, VCNC is applicable if a vibrational resonance of the molecule responds spectrally upon ordering or crystallization (Fig. 7). The vibrational spectra can then be simulated with varying l_d as the only fit parameter to measure the size of crystalline domains if the transition dipole orientations and their relative orientations $\hat{\mu}_i$ and positions $\vec{r}_{ij}$ are known for all molecules in a crystalline domain. Single-crystal x-ray diffraction (XRD), largely insensitive to point defects and small degrees of orientational disorder, provides the molecular (atomic) positions $\vec{r}_{ij}$, and $\hat{\mu}_i$ is obtained from normal mode analysis. FTIR absorption spectroscopy is applied to a dilute solution of the molecule with known concentration yielding $|\vec{\mu}|$ given by[66]

$$|\vec{\mu}| = \sqrt{\frac{3\epsilon_0 hc \ln 10}{2\pi^2 N_A \bar{\nu}} \int \epsilon(\nu) d\nu}, \tag{16}$$

where N_A is Avogadro's number, $\bar{\nu}$ is the center frequency of the resonance, and $\epsilon(\nu)$ is the extinction coefficient determined through Beer's law

$$A(\nu) = \epsilon(\nu) cl, \tag{17}$$

with c the concentration and l the optical path length through the solution. The values of $\hat{\mu}_i$ and $\vec{r}_{ij}$ derived from XRD on a highly ordered phase of the molecule of interest combined with $|\vec{\mu}|$ derived from FTIR on a completely amorphous phases are then used as input parameters to model the VE spectrum as a function of l_d. Measuring the vibrational response at many probe tip positions then images the macroscopic heterogeneity of l_d [see Fig. 6(e)] in partially ordered and disordered molecular solids such as polycrystalline films, aggregates, polymers, or other molecular complexes with mixed domains of order and disorder.

Applying this framework to RuOEP-DMPO, XRD was performed on single crystals to determine the crystal structure [Fig. 8(a)]. FTIR absorption spectroscopy of RuOEP-DMPO dissolved in dichloromethane at concentrations ranging from 2 to 20 mM determined $|\vec{\mu}|$ to be 1.43 Debye. These values were used as inputs to model the resulting VE nano-FTIR spectra for crystalline domains with varying number of molecules N [Fig. 8(b)]. Due to the specific structure of RuOEP-DMPO crystals, the carbonyl vibration shifts only up to $\sqrt[3]{N} = 3$ ($l_\mathrm{d} \approx 3$ nm) with $\Delta\tilde{\nu}_{\mathrm{model}}$ converging to 10.2 cm^{-1}, becoming independent of N for $\sqrt[3]{N} \geq 3$.[56] Since the VE shift is approximately constant already for small domains, the measured vibrational shift in RuOEP-DMPO crystals serves as a benchmark to validate VE modeling as a quantitative tool for measuring vibrational delocalization l_d and crystalline domain size.

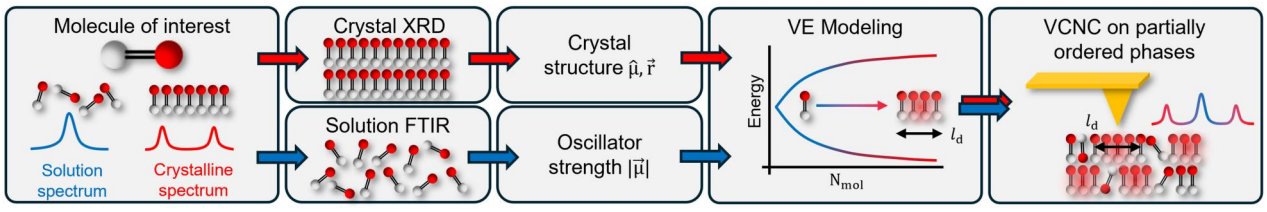

FIG. 7. Vibrational coupling infrared nano-crystallography (VCNC) applied to arbitrary molecular systems. If a vibrational mode of a molecule of interest exhibits frequency shifts or splitting upon crystallization, VCNC can be applied to study disorder in partially ordered phases of the molecule. First, the vibrational exciton modeling parameters are determined by performing XRD on single crystals to determine $\hat{\mu}$ and $\vec{r}$ of the primary crystalline phase, while FTIR absorption spectroscopy is performed on dilute solutions to determine $|\mu|$ of the isolated probe vibration. Vibrational exciton modeling can then be applied to relate measured vibrational shifts to the vibrational delocalization length l_d.

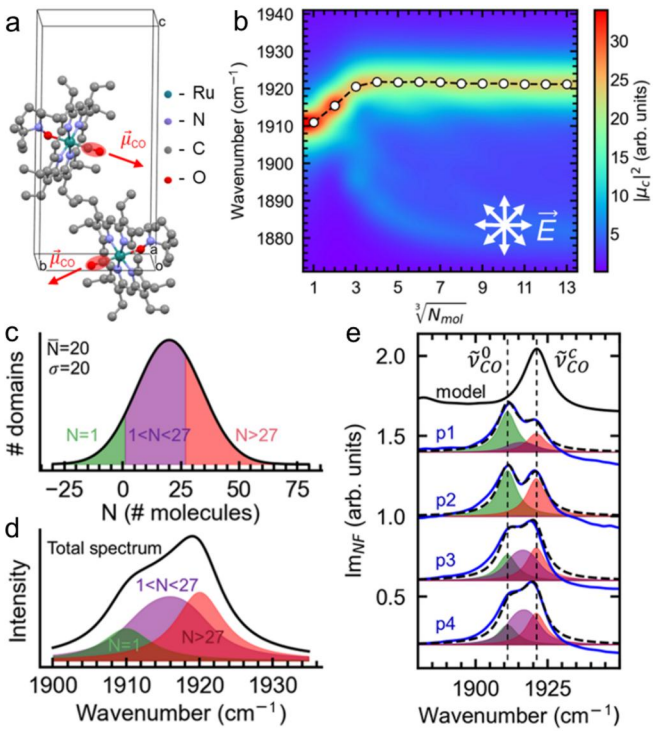

FIG. 8. VCNC analysis of nanoscale inhomogeneity in RuOEP-DMPO nano-crystals and films. (a) Molecular and crystal structures of RuOEP-DMPO from x-ray diffraction. The carbonyl ligand is highlighted in red, with arrows denoting the direction of the vibrational transition dipole $\vec{\mu}$. (b) Collective frequency shift $\tilde{\nu}^c_{CO}$ as a function of domain size ($\sqrt[3]{N}$) based on VE modeling. (c) Gaussian domain size distribution model with mean domain size $\bar{N} = 20$ and standard deviation $\sigma_N = 20$ separated into domains of single molecules (green), domains with short-range order (purple), and domains with long-range order (red). (d) Corresponding composite spectrum (black) with respective domain contributions (colored). (e) Gaussian model fit (black dotted) to measured IR *s*-SNOM spectra (blue) with corresponding spectral deconvolutions. Adapted with permission from Puro *et al.*, Nano Lett. **24**, 1909–1915 (2024).[56] Copyright 2024 American Chemical Society.

Measured vibrational nano-FTIR spectra of RuOEP-DMPO exhibit both the VE and amorphous carbonyl response, similar to the RuOEP derivative studied originally[29] [Fig. 8(e)]. However, unlike previous studies assuming homogeneity within the near-field sample region, a refined interpretation considers the signal as a superposition of responses from many domains of varying size. The domain sizes were assumed to follow a normal distribution [Fig. 8(c)]. Composite spectra were modeled by summing absorption features from many domains with corresponding VE center frequencies and normally distributed amplitudes [Fig. 8(d)]. Figures 8(c) and 8(d) divides the domain sizes into completely amorphous (green), intermediate (purple), and crystalline (red). Figure 8(e) shows fits (black dotted) to vibrational spectra measured on several crystals (blue) by fitting the large-domain frequency limit $\tilde{\nu}^c_{CO}$, average domain size $\bar{N}$, and its standard deviation σ with corresponding decomposition into each subset of domain sizes (green, purple, and red). The contribution from amorphous, intermediate, and crystalline domains varied significantly between crystals, providing additional insight into the sub-tip resolution structural composition. Moreover, the measured values of $\tilde{\nu}^c_{CO}$ agreed with $\Delta\tilde{\nu}_{model} = 10.2\ cm^{-1}$ to within modeling uncertainty for all measured crystals, demonstrating the high accuracy of VE modeling and thus the capacity of VCNC to qualitatively determine l_d.

These works have established the conceptual basis of applying VE nano-spectroscopy and imaging to relate coupling-induced vibrational frequency shifts to the delocalization length of the vibrational wavefunction l_d as a metric for the degree of local molecular order or disorder. Section IV describes recent works applying this technique of VCNC to molecular solids such as SAMs, molecular crystals, and protein complexes.

IV. VCNC APPLICATIONS

Unlike conventional techniques, which derive a net molecular arrangement from the spatially averaged ensemble response of a material, VCNC derives the spatially resolved nanoscale molecular arrangement from the local material response of molecular subensembles. Analyzing the nano-localized vibrational spectra with VE modeling, the vibrational delocalization length l_d can be extracted and related to the degree of local structural order, and its spatial heterogeneity imaged across macroscopic distances. Sections IV A–IV C describe example applications of VCNC to study the structure of molecular solids of different complexity, from monolayers to polymers and proteins. Section V then describes extensions of VCNC to study structural kinetics in dynamically evolving systems.

A. Molecular monolayer domain formation

Molecular arrangement in self-assembled monolayers (SAMs) plays a critical role in defining surface functionality across a range of applications—from molecular electronics to biosensing.[67,68] Even minor variations in molecular arrangement, such as defects or domain morphology, can significantly alter properties such as surface wetting, adhesion, and friction. However, probing the structural organization of SAMs, especially at buried interfaces or in kinetic environments, has remained a major experimental challenge. VE formation in 2D molecular systems provides a unique opportunity to resolve the structure of molecular monolayers on the nanoscale and in a minimally invasive fashion.

VCNC has been successfully applied to nano-image domain heterogeneity in SAMs of p-nitrothiophenol (pNTP) covalently bound to gold surfaces.[36] These monolayers spontaneously phase segregate into two types of domains with molecules oriented either in-plane or out-of-plane relative to the substrate plane[69] [Fig. 9(a)]. For VCNC, the symmetric nitro stretch mode with $\tilde{\nu}_0 = 1336\ cm^{-1}$ serves as the probe vibration with its vibrational wavefunction delocalizing across domains of similarly oriented molecules. The observed blue shift of the VE mode $\tilde{\nu}_c$ then reflects the underlying domain size (see Sec. II B for modeling details). Figure 9(b) shows examples of IR *s*-SNOM spectra measured at different sample locations indicated in Fig. 9(c) and their corresponding Lorentzian fits providing the center frequency $\tilde{\nu}_c$ and linewidth Γ of the VE response.

The VE linewidth provides additional information about domain heterogeneity at even the sub-tip resolution length scale. Within the ~20 nm spatial resolution of IR *s*-SNOM, a single spectrum averages over $\sim 10^4$ molecules distributed across up to tens of few-nm^2 sized domains. If these domains vary widely in size or shape, the resulting nano-FTIR spectrum would exhibit significant

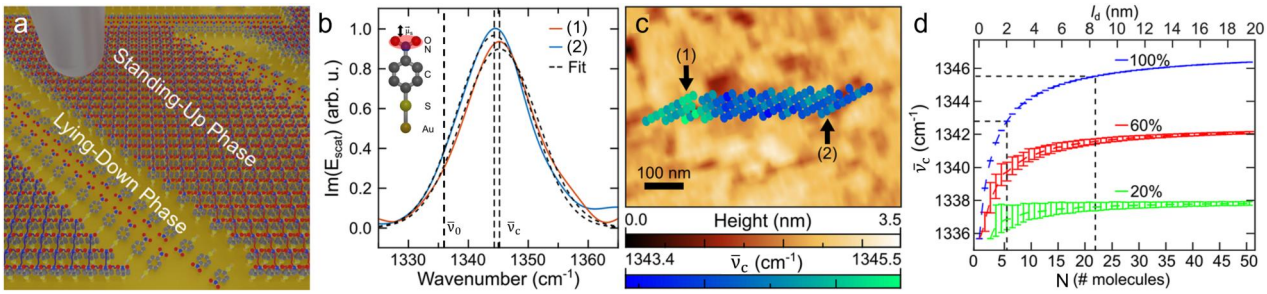

FIG. 9. VCNC applied to self-assembled monolayers (SAMs) of pNTP. (a) Domain formation in pNTP SAMs with molecules phase separating into standing up and lying down phases. (b) Representative NO_2 symmetric stretch mode of pNTP with coupled-mode frequency $\tilde{\nu}_c$ blue shifted by 7–9 cm^{-1} compared to uncoupled $\tilde{\nu}_0 = 1336\ cm^{-1}$. (c) Nano-imaging of $\tilde{\nu}_c$ with VE shifts correlated with l_d by (d) VE modeling of pNTP domains with varying NO_2 filling fraction ranging from 20% (green) to 100% (blue). Reproduced with permission from Gray *et al.*, Nano Lett. **21**, 5754–5759 (2021).[36] Copyright 2021 American Chemical Society.

inhomogeneous broadening. However, measured spectra of pNTP monolayers exhibited values of Γ nearly identical to the uncoupled symmetric stretch mode, suggesting that the domains are relatively homogeneous in size and shape at the 20 nm scale [Fig. 9(b)]. Despite this homogeneity on nanometer length scales, imaging of $\tilde{\nu}_c$ shows that the average domain sizes vary spatially over 100's of nanometers [Fig. 9(c)]. Using VE modeling to derive l_d from $\tilde{\nu}_c$. Figure 9(d) shows the results of VE modeling relating $\tilde{\nu}_c$ to l_d for various filling fractions. The NO_2 filling fraction was controlled by diluting pNTP with thiophenol, used to calibrate the magnitude of the NO_2 transition dipole.[36] The 100% filling fraction (blue) is relevant for the SAMs shown in Figs. 9(b) and 9(c). Domains were found to range in size between 2 and 8 nm in lateral extent (~4–64 nm^2), in agreement with STM imaging,[69] demonstrating the ability of VCNC to accurately determine the size of sub-tip resolution molecular domains and their heterogeneity across a range of length scales.

B. Polymer morphology and crystallinity

In crystalline solids, vibrational coupling effects are particularly pronounced. Classic examples include crystalline polymers such as poly(ethylene oxide) (PEO), poly(oxymethylene) (POM), and poly(tetrafluoroethylene) (PTFE, commonly known as Teflon), which exhibit changes to the vibrational spectrum in the 900–1200 cm^{-1} spectral range (CF_2 or C-O-C stretch modes), depending on the tertiary structure and crystallite shape (e.g., needlelike crystals with $R \ll H$ compared to lamellar crystals with $R \gg H$).[38–40] Transition dipole coupling models were able to qualitatively describe the observed trends in vibrational frequencies[41] associated with average polymer crystal structure and orientation to be determined spectroscopically from macroscopic ensemble measurements.

In polymers, chain conformation and crystalline ordering critically influence macroscopic properties.[70–72] They exhibit a wide range of morphologies, from amorphous glasses to semi-crystalline frameworks, each with distinct mechanical, electronic, and chemical properties. Among these, PTFE exhibits a particularly complex phase behavior arising from its helical geometry and strong C–F bonds, resulting in multiple crystalline phases and conformational transitions dependent on temperature and processing conditions.[73,74] The characteristic C–F stretch and bend vibrational modes provide spectroscopic signatures sensitive to these structural variations, enabling molecular-level insights into chain orientation and packing. To directly visualize how these vibrational features correlate with nanoscale crystal morphology, VCNC has been applied to semi-crystalline PTFE[57] [see AFM image, Fig. 10(a), lower panels]. By imaging the VE-induced spectral shifts of the C–F stretch vibrations, the nanoscale spatial variations in crystallinity could be resolved.

Using broadband femtosecond IR *s*-SNOM, the symmetric ($\tilde{\nu}_s \sim 1220\ cm^{-1}$) and antisymmetric ($\tilde{\nu}_{as} \sim 1155\ cm^{-1}$) C–F stretch modes are probed simultaneously, whose VE-induced frequency shifts sensitively report changes in local morphology and crystallinity. Hyperspectral nano-FTIR imaging of center frequency $\tilde{\nu}$, linewidth Γ, and amplitude A of $\tilde{\nu}_s$ and $\tilde{\nu}_{as}$ across many PTFE crystallites is shown in Fig. 10(a) (upper panels) for $\tilde{\nu}_{as}$. Strong correlations between $\tilde{\nu}_s$ and $\tilde{\nu}_{as}$, both varying spatially across the crystalline complex with frequency shifts exceeding 20 cm^{-1} across individual crystallites [Fig. 10(b)], reflect strong and correlated intrachain and interchain VE coupling. Based on topography, the density map of spectral shifts of $\tilde{\nu}_s$ and $\tilde{\nu}_{as}$ can be separated into interfacial (blue) and bulk regions (red) of the polymer crystallites. Here, regions with higher degree of local order exhibit a redshift with more narrow linewidths and narrower spectral distribution, whereas disordered or interfacial regions are indicated by a blueshift with broader linewidth and broader spectral distribution. The correlated $\tilde{\nu}_s$ and $\tilde{\nu}_{as}$ shifts thus provided a spectral fingerprint of the degree of intrachain and interchain order.[57]

To further interpret the observed spectral variations, density-functional-theory (DFT) calculations on isolated and crystalline PTFE chains parameterizing a VE Hamiltonian describing through-bond and through-space C–F coupling reproduce the experimentally observed correlated shifts of $\tilde{\nu}_s$ and $\tilde{\nu}_{as}$ depending on packing and chain location within a crystalline filament [Fig. 10(c)]. Chains located near the surface experience weaker coupling with smaller vibrational blue shifts of ~4–7 cm^{-1} relative to those near the crystal interior. The simulations thereby link spatially dependent vibrational frequencies to molecular packing, revealing that the experimentally observed spectral heterogeneity originates from a combination of intra- vs interchain coupling, phase coexistence, and local disorder within the crystalline filaments.

Complementary four-dimensional scanning transmission electron microscopy (4D-STEM) reveals the associated nano-crystal orientation and long-range structural correlations [Fig. 10(d)]. Flowline orientation maps and radial autocorrelation analysis demonstrate that

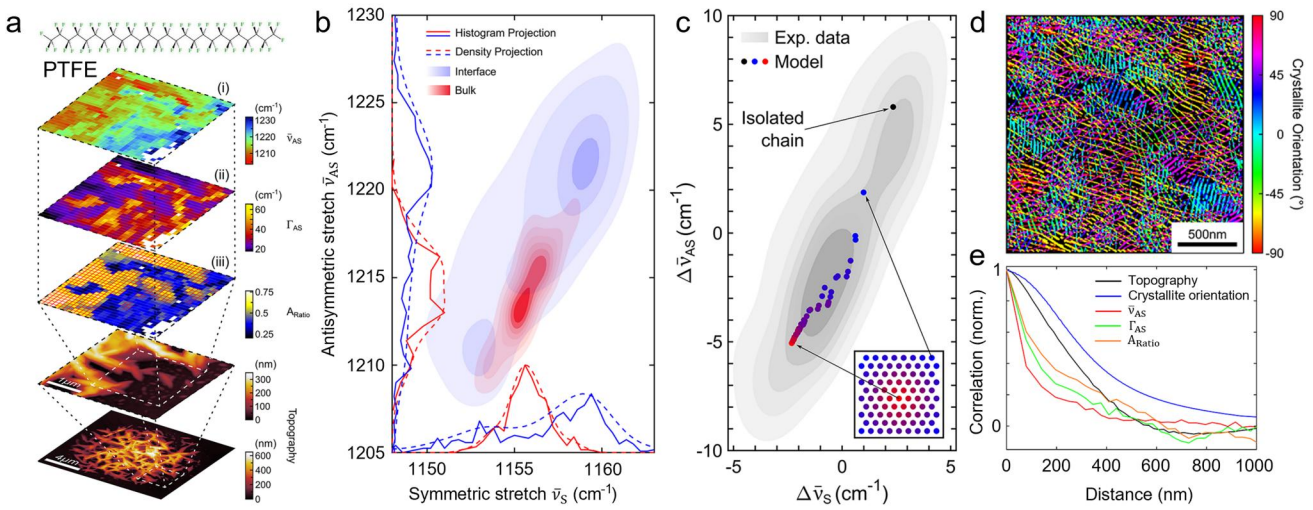

FIG. 10. Vibrational exciton formation in polycrystalline PTFE. (a) Nano-FTIR imaging of the center frequency $\tilde{\nu}_{as}$, linewidth Γ_{as}, and amplitude A_{as} of the asymmetric CF_2 vibrational mode with AFM topography. (b) Histogram representing spectral shifts in $\tilde{\nu}_s$ and $\tilde{\nu}_{as}$ across PTFE crystallites with interfacial regions (blue) separated from bulk regions (red) based on the topographic height of each image pixel. (c) Modeled shifts in $\tilde{\nu}_{as}$ and $\tilde{\nu}_s$ vibrational modes for chains located in the center vs the exterior of individual crystallites. PTFE chains located in the center exhibit larger shifts compared to interfacial chains due to their different number of neighboring vibrational oscillators. (d) Flowline chart of crystallite orientation from corresponding 4D-STEM measurements. (e) Radial autocorrelation of structural (topography, crystal orientation) and spectral parameters ($\tilde{\nu}_{as}$, Γ_{as}, and $A_{Ratio} = A_s/A_{as}$). Adapted with permission from Donges *et al.*, Nano Lett. **21**, 6463–6470 (2021).[57] Copyright 2021 American Chemical Society.

crystallite orientation is correlated over distances exceeding 300–400 nm—significantly longer than the 150–200 nm correlation lengths derived from vibrational frequency shifts in spatio-spectral *s*-SNOM imaging [Fig. 10(e)]. This apparent discrepancy indicates that although PTFE crystallites share common lattice orientation across extended regions, substantial internal disorder and heterogeneous coupling exist within each crystallite. Together, the combined VCNC, DFT modeling, and 4D-STEM results reveal a hierarchical structural organization in PTFE where nanoscale vibrational heterogeneity is embedded within a framework of mesoscopic crystalline alignment, providing a comprehensive picture of how local disorder modulates macroscopic order. Although demonstrated at the example of PTFE, VCNC is generally applicable to any polymer with suitably strong and coupled vibrational resonances. In combination with other structurally sensitive techniques, VCNC could contribute to multiscale insight into the complex hierarchical order of synthetic and natural polymers.

C. Protein secondary and tertiary structure

In structural biology, the relationship between molecular function and structure is paramount. Proteins and other biomolecules often undergo conformational changes that directly influence their activity.[75–77] The secondary protein structures, such as α-helix and β-sheet, stabilized by hydrogen bonding between backbone amide groups,[78] depend on the local chemical environment, requiring tools that can probe the protein conformation *in situ* and across timescales of protein kinetics. In that regard, VCNC can complement the established techniques of x-ray diffraction (XRD) and cryo-electron microscopy (cryo-EM)[30,79,80] for resolving biomolecular structures.

In parallel to the development of VE theory, shifts in the amide-I spectral response at $\sim$1650 cm^{-1} of proteins and polypeptides were correlated qualitatively with secondary structures of α-helixes and β-sheets (and to a lesser extent tertiary structures).[81] In 1960, a perturbation-based theory to explain these frequency shifts was proposed in terms of through-bond (intrachain) and hydrogen bond (interchain) interactions between amide groups on neighboring peptide units.[82] This model, however, was later shown to require unphysically large through-bond interaction constants. In response, a refined model was introduced incorporating TDC between spatially distant peptide units.[23] This framework, accounting for TDC and both through-bond coupling and H-bonding, has become the prevailing explanation for secondary and tertiary structure-related vibrational frequency shifts in proteins and polypeptides.[24,83]

Ultrafast linear and nonlinear IR techniques have been used in the far field to investigate the secondary structure of proteins.[45,48] The VE Hamiltonian can be parameterized using input geometries derived from molecular dynamics (MD) simulations or density-functional-theory (DFT) calculations.[46,47] Although IR spectroscopy lacks the level of structural detail compared to NMR or XRD, it readily distinguishes between common secondary structures such as parallel and antiparallel β-sheets, α-helices, or DNA base-pairing motifs[84] yet provides high temporal resolution.

Recent advancements in VCNC have enabled high-resolution spatial mapping of proteins with different structures distinguishable by their vibrational response.[65,85,86] VCNC can access both inter- and intramolecular coupling as shown at the example of 2D peptoid sheets and 3D catalase crystals[65] [Fig. 11(a)]. In 2D peptoid films, terraced domains of varying thickness can be spectroscopically distinguished with monolayer resolution.[65] Here, blue shifts in the amide-I band correlate with increasing thickness was attributed to interlayer coupling, while concurrent linewidth changes suggested substrate-induced perturbations even at the monolayer level. This ability to

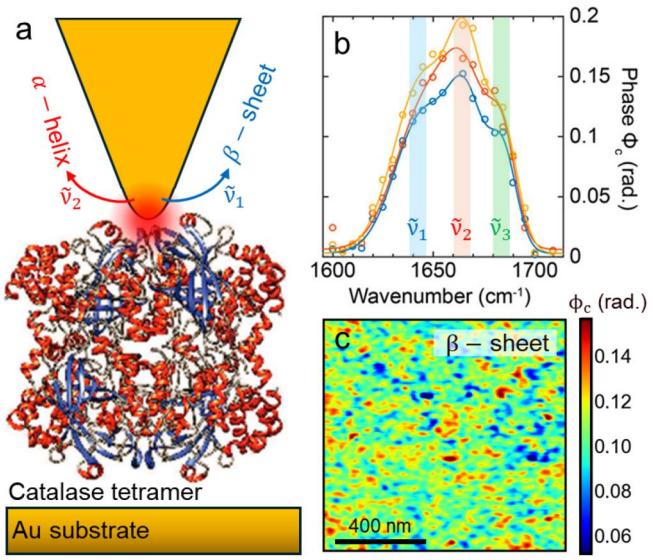

FIG. 11. Vibrational coupling in proteins. (a) IR *s*-SNOM of catalase crystals with mixed β-sheet and α-helix moieties, distinguishable by their amide-I frequencies $\tilde{\nu}_1$ and $\tilde{\nu}_2$ respectively. (b) Vibrational spectra in the amide-I spectral region measured at three different locations showing features attributed to β-sheet ($\tilde{\nu}_1$, blue), α-helix ($\tilde{\nu}_2$, red), and random coil moieties ($\tilde{\nu}_3$, green). (c) Single-frequency nano-imaging of catalase crystals at $\tilde{\nu} = 1625\,\mathrm{cm}^{-1}$ to identify the β-sheet moiety. Reproduced with permission from O'Callahan *et al.*, J. Phys. Chem. C **122**, 24891–24895 (2018).[65] Copyright 2018 American Chemical Society.

distinguish protein–protein vs protein–substrate interactions points toward a powerful new means of tailoring protein function through surface engineering.

In 3D catalase crystals [Fig. 11(a)], VCNC revealed significant heterogeneity in the amide-I region across sub-diffraction-limited regions.[65] Three distinct features were present in the vibrational spectrum [Fig. 11(b)], attributed to β-sheet ($\tilde{\nu}_1$, blue), α-helix ($\tilde{\nu}_2$, red), and random coil moieties ($\tilde{\nu}_3$, green). Selected frequency IR *s*-SNOM of the catalase crystals then imaged the relative density of each moiety by tuning the excitation wavelength to the vibrational resonance of each secondary structure. Figure 11(c) shows an IR *s*-SNOM image at $1625\,\mathrm{cm}^{-1}$, selecting the β-sheet secondary structure and revealing significant heterogeneity in its density across the catalase crystal. The results support the hypothesis that even nominally single protein crystals can exhibit conformational heterogeneity at the nanoscale.

With further development—particularly toward measurements in aqueous environments[87,88] and ultrafast studies[89,90]—VCNC may become an important tool for studying the dynamics and heterogeneity of functional biological systems. Looking further, the development of nonlinear near-field infrared spectroscopy (nano-2DIR) would enable the ultrafast dynamics of the intermolecular coupling mechanisms to be probed with nanoscale spatial resolution.[91]

V. KINETIC PROCESSES

Nanoscale studies of VE coupling have successfully derived the degree of disorder within molecular systems ranging from 2D SAMs to polymer and protein poly-crystals. In static systems, l_d is measured for nanometer-sized molecular ensembles, and its heterogeneity is imaged spatially across micrometer length scales. Another important dimension is understanding the structure and kinetic evolution of molecular systems as a function of, e.g., temperature, solvent environment, or chemical reactions including phase transitions or melting. VCNC can be applied to determine nanoscale structural information in dynamically evolving systems.[21,22,43] Sections V A and V B describe applications of VCNC to probe temporal evolution of nanoscale structure in the molecular systems previously studied statically.

A. Crystallization and phase transitions

Molecular crystals can undergo a wide range of morphological changes as a function of temperature or solvent annealing. As an example, introduced in Sec. III, crystals of the metalloporphyrin complex RuOEP were grown in a P3HT matrix.[29] Under solvent vapor, the RuOEP molecules diffuse through the polymer matrix and nucleate resulting in crystal growth, Ostwald ripening, and subsequent increase in degree of crystallinity through solvent annealing. Studying several RuOEP crystals, crystallinity and l_d generally increase and the overall structural heterogeneity decreases with annealing time [Figs. 12(a) and 12(c)]. This ability to determine nanoscale structural information during crystal growth or material synthesis can be applied to a wide range of molecular systems to inform growth parameters optimizing crystallinity and crystal size.

Similarly, VCNC has been applied to study the thermally induced conformational changes in PTFE. Heating PTFE from 10 to 40 °C induces a structural phase transition associated with an untwisting of the PTFE helical conformation from a noncommensurable 13_6 configuration (form II) to a commensurable 15_7 configuration (form IV).[92] This is reflected by a corresponding change in linewidth (Γ_{as}) and frequency of the asymmetric CF_2 vibrational mode $\tilde{\nu}_{as}$ [Fig. 12(d)]. The correlated increase in Γ_{as} and blue shift of $\tilde{\nu}_{as}$ agree well with VE modeling of the two structural configurations of PTFE. The results demonstrate that VCNC can track temperature-dependent phase transitions in molecular solids.

B. Chemical composition and transformations

Far-field spectroscopy of VE-induced frequency shifts in 2D molecular SAMs has been used to monitor structural transitions such as the monolayer formation of CO chemisorbed on metal surfaces[93] and CO_2 adsorbed on NaCl.[43,44] VE formation enables probing the monolayer structure including filling fraction and molecular orientation, which can be tracked as a function of temperature and pressure. VE formation also tracks kinetics in, e.g., poly(ethylene glycol) monolayers grown from solution onto gold substrates where vibrational resonances in the fingerprint region narrow as molecules align.[22,41] Probing the evolution of monolayer structure in *situ* and in changing environments is desirable for understanding their performance.

In VCNC of SAMs of pNTP, dilute monolayers were synthesized by spacing the coupling NO_2 vibrations using thiophenol [Fig. 13(a)].[36] This allows for the VE coupling efficiency to be tuned by varying the concentration of NO_2 oscillators, leading to a gradual blue shift of the NO_2 symmetric bend vibration with increasing NO_2 oscillator density [Figs. 13(b) and 13(c)], as expected due to the increasing coupling efficiency.

The ability to determine the concentration of NO_2 oscillators from their vibrational spectra further enables vibrational coupling to

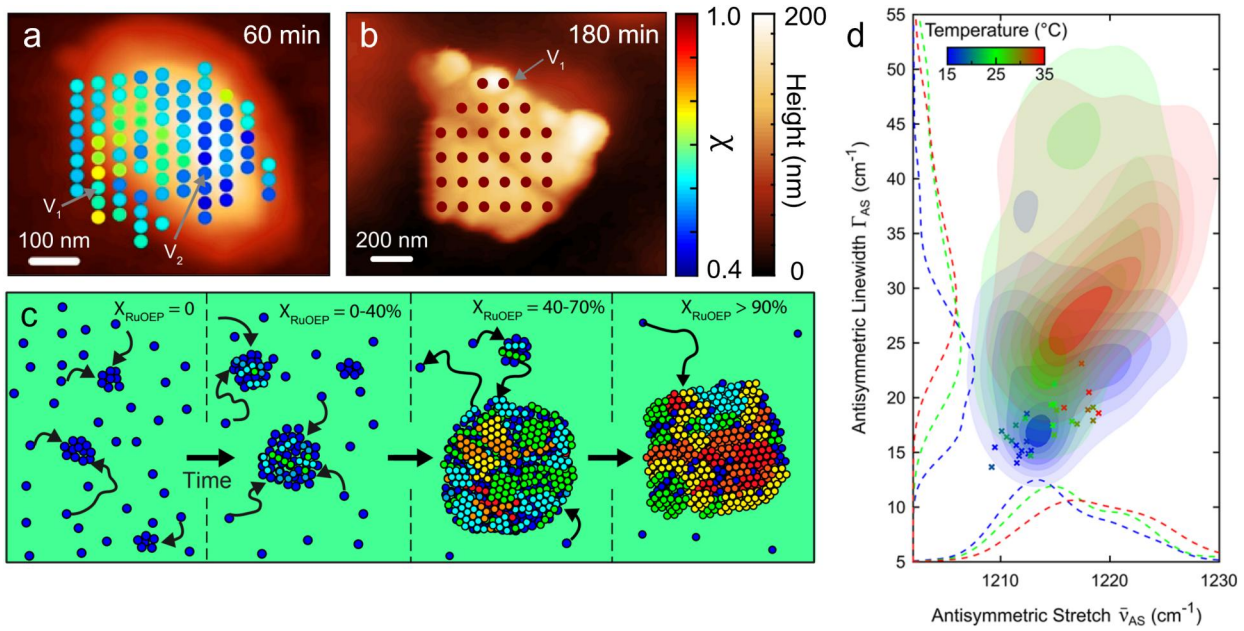

FIG. 12. Crystal growth and molecular ordering. (a) VCNC imaging of crystallinity in RuOEP crystals solvent annealed for 60 min and (b) annealed for 180 min. (c) Schematic of Ostwald ripening and crystal growth during solvent annealing. Dark blue circles indicate amorphous RuOEP, light blue through red circles indicate ordering. (d) Temperature-dependent density correlation of $\tilde{\nu}_{as}$ and Γ_{as} in PTFE crystals showing an overall blueshift and broadening of the vibrational exciton peak with increasing temperature. Panels (a)–(c) are adapted with permission from Muller *et al.*, Proc. Natl. Acad. Sci. U. S. A. **117**, 7030–7037 (2020). Copyright 2020 Authors, licensed under CC BY 4.0.[29] Panel (d) is reproduced with permission from Donges *et al.*, Nano Lett. **21**, 6463–6470 (2021).[57] Copyright 2021 American Chemical Society.

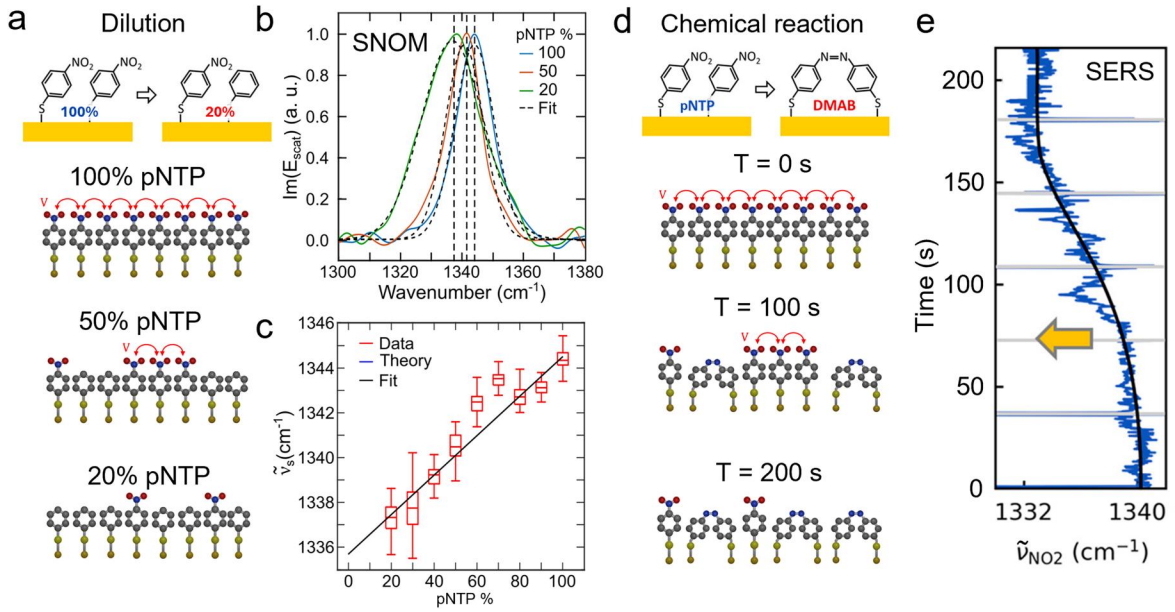

FIG. 13. Vibrational coupling used to track dilution of NO_2 oscillators in pNTP self-assembled monolayers (SAMs). (a) Dilution of NO_2 oscillators by synthesizing SAMs mixing thiophenol and pNTP. (b) Representative nano-FTIR spectra of SAMs with pNTP concentration ranging from 100% to 20% and (c) corresponding tuning curve of NO_2 symmetric stretch center frequency exhibiting a blue shift with increasing pNTP concentration due to increased coupling. (d) Reduction of NO_2 groups by a dimerization. (e) Evolution of the NO_2 symmetric stretch frequency over the course of the reaction exhibiting a red shift as the NO_2 density decreases. Panels (b) and (c) are adapted with permission from Gray *et al.*, Nano Lett. **21**, 5754–5759 (2021).[36] Copyright 2021 American Chemical Society. Panels (d) and (e) are adapted with permission from Mueller *et al.*, Nano Lett. **22**, 7254–7260 (2022). Copyright 2022 Authors, licensed under CC BY 4.0.[37]

track a dimerization reaction in pNTP SAMs.[37] Monolayers of pNTP on metal substrates were probed using surface-enhanced Raman spectroscopy (SERS) to follow the chemical reaction. As the density of NO_2 vibrations decreases, the symmetric stretch vibration red-shifts toward its uncoupled frequency, providing a quantitative measure of the reaction rate [Figs. 13(d) and 13(e)]. These studies underscore the utility of vibrational coupling as both a structural and chemical reporter also for kinetic processes.

VI. CONCLUSION AND PERSPECTIVE

In this final section, we provide a summary of vibrational exciton (VE) nano-spectroscopy and nano-imaging with a perspective for the future development of the field. VEs, arising from hybridization of vibrational modes due to transition dipole coupling, have been observed across a broad range of ordered and disordered molecular systems, including molecular crystals, self-assembled monolayers, molecular liquids, and biomolecules. The associated vibrational wavefunction delocalization leads to the formation of collective vibrational states, known as VEs, which manifest as characteristic spectral shifts and mode splittings in mid-infrared vibrational spectra. These spectral signatures encode information about molecular packing, orientation, and local disorder, enabling the inference of structural characteristics from vibrational measurements alone. When combined with VE modeling, infrared spectroscopy becomes a powerful tool for probing molecular conformation and structural dynamics across time scales ranging from femtoseconds to hours.

Extending far-field spectroscopy of VEs to the nanoscale, applying VE modeling to interpret infrared scattering-type scanning near-field optical microscopy (IR *s*-SNOM) spectra enables direct spatial mapping of vibrational coupling and energy delocalization with few-nanometer spatial and sub-wavenumber spectral precision. In this method of vibrational coupling nano-crystallography (VCNC), the extent of vibrational delocalization within the near-field probe volume serves as a molecular ruler for imaging morphological order and disorder with spatial resolution down to ∼20 nm and sensitivity to as few as ∼100 oscillators.[36]

VCNC has already demonstrated its utility to probe nanoscale morphology of several molecular systems, including porphyrin nanocrystals,[29,56] protein complexes,[65] polycrystalline polymers,[57] and self-assembled molecular monolayers.[36] In each case, shifts in the VE spectra have been used to infer domain size, local crystallinity, and conformational heterogeneity. In molecular solids where the crystalline domains are much smaller than the tip resolution, VCNC provides sub-tip resolution structural information by interpreting the VCNC spectra as a statistical distribution of domain sizes[56] (see Sec. 3.3.2). In solids where the domains are much larger than the tip resolution, VCNC spectral shifts vary depending on proximity to a crystalline interface providing a spectroscopic distinction between bulk and interfacial regions[57] (see Sec. 4.4.2).

Unlike x-ray or electron diffraction, VCNC excels in characterizing partial order and nanoscale disorder in small crystalline domains or disordered interfaces. VCNC leverages the known or modeled packing structure of the fully crystalline phase, e.g., determined by single-crystal XRD, to then extract spatial variations in local order from spatio-spectral nano-imaging of partially disordered, polycrystalline, or amorphous phases of the material.

Beyond IR *s*-SNOM, several other near-field spectroscopy methods may also be adapted to perform VCNC. Since coupling-induced vibrational frequency shifts equally manifest in vibrational Raman spectra of VE materials,[37] VCNC could be performed with tip-enhanced Raman scattering (TERS) with the additional benefit of the higher symmetry selectivity of the Raman tensor.[94] Photothermal AFM-IR and photo-induced force microscopy (PiFM) would also be sensitive to coupling-induced shifts in the vibrational response. The application of VE modeling to interpret vibrational frequency shifts measured through any of these techniques can provide insights into the nanoscale morphology of order and disorder in molecular solids as demonstrated thus far with IR *s*-SNOM.

VCNC holds significant promise for characterizing materials whose macroscopic function depends critically on nanoscale molecular order. In particular, molecular electronic and organic optoelectronic materials for photovoltaic, light-emitting, and other devices often rely on polycrystalline films formed via solution processing.[7] In these systems, VCNC could be employed to correlate charge carrier mobility with local vibrational delocalization, shedding light on how nanoscale structure influences bulk performance. Additionally, integrating VCNC with ultrafast pump–probe spectroscopy[89,90] would enable simultaneous tracking of excited-state electron dynamics and its dependence on molecular order and intermolecular coupling. For instance, one could probe how photo-induced changes in vibrational coupling correlate with charge transport or reactivity, or how VE behavior evolves following electronic or vibrational excitation.

Looking ahead, continued developments in near-field microscopy promise to open new frontiers for nanoscale VE spectroscopy. VCNC under cryogenic conditions could reveal coherent vibrational dynamics obscured by thermal disorder,[95–97] while measurements at solid–liquid interfaces or within aqueous environments may capture dynamic interfacial dynamics. The application of electric fields for vibrational Stark tuning or other external perturbations opens additional degree of freedom to interface with VE nano-spectroscopy modifying the VE state. In addition, cavity, IR antenna, or metasurface coupling can provide control over the evolution of the VE as a collective vibrational coherent state, which may enable quantum sensing, transduction, and control with molecular vibrations at infrared frequencies. As methods continue to mature, VCNC may also be extended to operate in buffered ionic or biologically relevant conditions.[87,88] Applications in live-cell imaging, heterogeneous catalysis, or soft-matter self-assembly may emerge, further positioning VCNC as a vital tool in the molecular sciences bridging the gap between structural precision and functional complexity.

ACKNOWLEDGMENTS

R.L.P. and M.B.R. acknowledge funding from the National Science Foundation (NSF Grant Nos. CHE 2512338 and CHE2108009), which supported the experimental part of this work, and from the U.S. Department of Energy, Office of Basic Sciences, under Award No. DE-SC0026055, which supported the extension of the theoretical concept.

AUTHOR DECLARATIONS

Conflict of Interest

The authors have no conflicts to disclose.

Author Contributions

Richard L. Puro: Conceptualization (equal); Investigation (equal); Methodology (equal); Writing – original draft (equal); Writing – review & editing (equal). **Markus B. Raschke:** Conceptualization (equal); Investigation (equal); Methodology (equal); Supervision (equal); Writing – original draft (equal); Writing – review & editing (equal).

DATA AVAILABILITY

The data that support the findings of this study are available from the corresponding author upon reasonable request.

REFERENCES

[1]Y. L. Chang, M. A. West, F. W. Fowler, and J. W. Lauher, "An approach to the design of molecular solids. Strategies for controlling the assembly of molecules into two-dimensional layered structures," J. Am. Chem. Soc. **115**, 5991–6000 (1993).

[2]H. Oberhofer, K. Reuter, and J. Blumberger, "Charge transport in molecular materials: An assessment of computational methods," Chem. Rev. **117**, 10319–10357 (2017).

[3]M. B. Ross, J. C. Ku, V. M. Vaccarezza, G. C. Schatz, and C. A. Mirkin, "Nanoscale form dictates mesoscale function in plasmonic DNA–nanoparticle superlattices," Nat. Nanotechnol. **10**, 453–458 (2015).

[4]A. Gumyusenge *et al.*, "Semiconducting polymer blends that exhibit stable charge transport at high temperatures," Science **362**, 1131–1134 (2018).

[5]J. B. Silva *et al.*, "Investigation of the structural, thermal, vibrational, and thermodynamic properties of olanzapine and risperidone crystals," J. Mol. Struct. **1365**, 146017 (2026).

[6]S. E. Root, S. Savagatrup, A. D. Printz, D. Rodriquez, and D. J. Lipomi, "Mechanical properties of organic semiconductors for stretchable, highly flexible, and mechanically robust electronics," Chem. Rev. **117**, 6467–6499 (2017).

[7]O. Ostroverkhova, "Organic optoelectronic materials: Mechanisms and applications," Chem. Rev. **116**, 13279–13412 (2016).

[8]S. O. Frimpong *et al.*, "Temperature-dependent structural dynamics in covalent organic frameworks observed by cryogenic infrared spectroscopy," Phys. Chem. Chem. Phys. **26**, 22252–22260 (2024).

[9]S. Suleman, X. Cheng, M. Gu, and Y. Kim, "Covalent organic framework-based cathodes for beyond lithium-ion batteries," Commun. Mater. **6**, 78 (2025).

[10]M. Chafiq, A. Chaouiki, and Y. G. Ko, "Advances in COFs for energy storage devices: Harnessing the potential of covalent organic framework materials," Energy Storage Mater. **63**, 103014 (2023).

[11]A. J. Tan *et al.*, "Topological chaos in active nematics," Nat. Phys. **15**, 1033–1039 (2019).

[12]X. Mao *et al.*, "Self-assembled nanostructures in ionic liquids facilitate charge storage at electrified interfaces," Nat. Mater. **18**, 1350–1357 (2019).

[13]Z. Wang *et al.*, "Disorder induced power-law gaps in an insulator–metal Mott transition," Proc. Natl. Acad. Sci. U. S. A. **115**, 11198–11202 (2018).

[14]E. A. Muller, B. Pollard, and M. B. Raschke, "Infrared chemical nano-imaging: Accessing structure, coupling, and dynamics on molecular length scales," J. Phys. Chem. Lett. **6**, 1275–1284 (2015).

[15]S. D. Fried and S. G. Boxer, "Measuring electric fields and noncovalent interactions using the vibrational stark effect," Acc. Chem. Res. **48**, 998–1006 (2015).

[16]R. Hexter, "Intermolecular coupling of vibrations in molecular crystals: A vibrational exciton approach," J. Chem. Phys. **33**, 1833–1841 (1960).

[17]D. A. Dows, "Intermolecular coupling of vibrations in molecular crystals," J. Chem. Phys. **32**, 1342–1347 (1960).

[18]J. Decius, "Coupling of the out-of-plane bending mode in nitrates and carbonates of the aragonite structure," J. Chem. Phys. **23**, 1290–1294 (1955).

[19]H. Torii, "Extent of delocalization of vibrational modes in liquids as a result of competition between diagonal disorder and off-diagonal coupling," J. Phys. Chem. A **108**, 2103–2107 (2004).

[20]R. Signorell and M. Jetzki, "Vibrational exciton coupling in pure and composite sulfur dioxide aerosols," Faraday Discuss. **137**, 51–64 (2008).

[21]Z. Chen *et al.*, "Tracing the crystallization process of polyoxymethylene/poly (ethylene oxide) crystalline/crystalline blends by two-dimensional infrared correlation spectroscopy," Vib. Spectrosc. **62**, 299–309 (2012).

[22]M. Chávez *et al.*, "Characterization of a self-assembled monolayer of O-(2-mercaptoethyl)-O′-methyl-hexa (ethylene glycol) (EG7-SAM) on gold electrodes," J. Electroanal. Chem. **880**, 114892 (2021).

[23]Y. Abe and S. Krimm, "Normal vibrations of crystalline polyglycine I," Biopolymers **11**, 1817–1839 (1972).

[24]E. Małolepsza and J. E. Straub, "Empirical maps for the calculation of amide I vibrational spectra of proteins from classical molecular dynamics simulations," J. Phys. Chem. B **118**, 7848–7855 (2014).

[25]P. Hamm and M. Zanni, *Concepts and Methods of 2D Infrared Spectroscopy* (Cambridge University Press, 2011).

[26]F. Keilmann and R. Hillenbrand, "Near-field microscopy by elastic light scattering from a tip," Philos. Trans. R. Soc. London, Ser. A **362**, 787–805 (2004).

[27]J. M. Atkin, S. Berweger, A. C. Jones, and M. B. Raschke, "Nano-optical imaging and spectroscopy of order, phases, and domains in complex solids," Adv. Phys. **61**, 745–842 (2012).

[28]R. Hillenbrand, Y. Abate, M. Liu, X. Chen, and D. Basov, "Visible-to-THz near-field nanoscopy," Nat. Rev. Mater. **10**, 285 (2025).

[29]E. A. Muller *et al.*, "Vibrational exciton nanoimaging of phases and domains in porphyrin nanocrystals," Proc. Natl. Acad. Sci. U. S. A. **117**, 7030–7037 (2020).

[30]B. E. Warren, *X-Ray Diffraction* (Courier Corporation, 1990).

[31]G. Hiebert and D. Hornig, "A new tool for the study of crystalline spectra," J. Chem. Phys. **20**, 918–919 (1952).

[32]D. A. Dows, "Intermolecular coupling of vibrations in molecular crystals. II. Intermolecular forces in CH_3CL and CD_3CL," J. Chem. Phys. **35**, 282–287 (1961).

[33]D. A. Dows, "Intermolecular coupling of vibrations in molecular crystals. III. Intermolecular potential and crystal structure of ethylene," J. Chem. Phys. **36**, 2836–2842 (1962).

[34]E. Bernstein, S. Colson, R. Kopelman, and G. Robinson, "Electronic and vibrational exciton structure in crystalline benzene," J. Chem. Phys. **48**, 5596–5610 (1968).

[35]R. Signorell, "Verification of the vibrational exciton approach for co_2 and n_2o nanoparticles," J. Chem. Phys. **118**, 2707–2715 (2003).

[36]T. P. Gray, J. Nishida, S. C. Johnson, and M. B. Raschke, "2D vibrational exciton nanoimaging of domain formation in self-assembled monolayers," Nano Lett. **21**, 5754–5759 (2021).

[37]N. S. Mueller *et al.*, "Collective mid-infrared vibrations in surface-enhanced Raman scattering," Nano Lett. **22**, 7254–7260 (2022).

[38]M. Shimomura, Y. Tanabe, Y. Watanabe, and M. Kobayashi, "Vibrational spectroscopic study on poly (ethylene oxide) crystals," Polymer **31**, 1411–1414 (1990).

[39]M. Kobayashi, H. Morishita, M. Shimomura, and M. Iguchi, "Vibrational spectroscopic study on the solid-state phase transition of poly (oxymethylene) single crystals from the orthorhombic to the trigonal phase," Macromolecules **20**, 2453–2456 (1987).

[40]M. Kobayashi, M. Sakashita, and M. Kobayashi, "Morphology-dependent anomalous frequency shifts of IR bands in polar polymer crystals: Polytetrafluoroethylene," Rep. Prog. Polym. Phys. Jpn. **34**, 347–350 (1991).

[41]M. Kobayashi and M. Sakashita, "Morphology dependent anomalous frequency shifts of infrared absorption bands of polymer crystals: Interpretation in terms of transition dipole–dipole coupling theory," J. Chem. Phys. **96**, 748–760 (1992).

[42]Ó. F. Sigurbjörnsson, G. Firanescu, and R. Signorell, "Vibrational exciton coupling as a probe for phase transitions and shape changes of fluoroform aerosol particles," Phys. Chem. Chem. Phys. **11**, 187–194 (2009).

[43]O. Berg, R. Disselkamp, and G. E. Ewing, "Anharmonic libration of Co_2 in domains on NaCl (100)," Surf. Sci. **277**, 8–20 (1992).

[44]J. Vogt, "CO_2 ultrathin film growth on a monolayer of co_2 adsorbed on the NaCl (100) surface: Sticking coefficient and IR-optical signatures in the ν_3 region," Phys. Chem. Chem. Phys. **26**, 21019–21029 (2024).

[45]A. Moran and S. Mukamel, "The origin of vibrational mode couplings in various secondary structural motifs of polypeptides," Proc. Natl. Acad. Sci. U. S. A. **101**, 506–510 (2004).

[46]P. Mukherjee, I. Kass, I. T. Arkin, and M. T. Zanni, "Picosecond dynamics of a membrane protein revealed by 2D IR," Proc. Natl. Acad. Sci. U. S. A. **103**, 3528–3533 (2006).
[47]P. Mukherjee, I. Kass, I. T. Arkin, and M. T. Zanni, "Structural disorder of the CD3ζ transmembrane domain studied with 2D IR spectroscopy and molecular dynamics simulations," J. Phys. Chem. B **110**, 24740–24749 (2006).
[48]C. Zscherp and A. Barth, "Reaction-induced infrared difference spectroscopy for the study of protein reaction mechanisms," Biochemistry **40**, 1875–1883 (2001).
[49]K. Ataka, T. Kottke, and J. Heberle, "Thinner, smaller, faster: IR techniques to probe the functionality of biological and biomimetic systems," Angew. Chem., Int. Ed. **49**, 5416–5424 (2010).
[50]A. Savara and E. Weitz, "Elucidation of intermediates and mechanisms in heterogeneous catalysis using infrared spectroscopy," Annu. Rev. Phys. Chem. **65**, 249–273 (2014).
[51]V. A. Lorenz-Fonfria, "Infrared difference spectroscopy of proteins: From bands to bonds," Chem. Rev. **120**, 3466–3576 (2020).
[52]D. Buhrke *et al.*, "Transient 2D IR spectroscopy and multiscale simulations reveal vibrational couplings in the cyanobacteriochrome Slr1393-g3," J. Am. Chem. Soc. **145**, 15766–15775 (2023).
[53]A. F. T. Waffo *et al.*, "Structural determinants of the catalytic Ni_a-L intermediate of [NiFe]-hydrogenase," J. Am. Chem. Soc. **145**, 13674–13685 (2023).
[54]R. A. Livingstone, Y. Nagata, M. Bonn, and E. H. Backus, "Two types of water at the water–surfactant interface revealed by time-resolved vibrational spectroscopy," J. Am. Chem. Soc. **137**, 14912–14919 (2015).
[55]S. Nihonyanagi, J. A. Mondal, S. Yamaguchi, and T. Tahara, "Structure and dynamics of interfacial water studied by heterodyne-detected vibrational sum-frequency generation," Annu. Rev. Phys. Chem. **64**, 579–603 (2013).
[56]R. L. Puro, T. P. Gray, T. A. Kapfunde, G. B. Richter-Addo, and M. B. Raschke, "Vibrational coupling infrared nanocrystallography," Nano Lett. **24**, 1909–1915 (2024).
[57]S. A. Donges *et al.*, "Multidimensional nano-imaging of structure, coupling, and disorder in molecular materials," Nano Lett. **21**, 6463–6470 (2021).
[58]J. M. Larson, H. A. Bechtel, and R. Kostecki, "Detection and signal processing for near-field nanoscale Fourier transform infrared spectroscopy," Adv. Funct. Mater. **34**, 2406643 (2024).
[59]H. A. Bechtel, S. C. Johnson, O. Khatib, E. A. Muller, and M. B. Raschke, "Synchrotron infrared nano-spectroscopy and-imaging," Surf. Sci. Rep. **75**, 100493 (2020).
[60]B. L. Esses *et al.*, "Ultrafast nano-imaging and nano-spectroscopy," Nat. Rev. Methods Primers **6**, 21 (2026).
[61]M. B. Raschke and C. Lienau, "Apertureless near-field optical microscopy: Tip–sample coupling in elastic light scattering," Appl. Phys. Lett. **83**, 5089–5091 (2003).
[62]A. Cvitkovic, N. Ocelic, and R. Hillenbrand, "Analytical model for quantitative prediction of material contrasts in scattering-type near-field optical microscopy," Opt. Express **15**, 8550–8565 (2007).
[63]P. McArdle, D. Lahneman, A. Biswas, F. Keilmann, and M. Qazilbash, "Near-field infrared nanospectroscopy of surface phonon-polariton resonances," Phys. Rev. Res. **2**, 023272 (2020).
[64]A. A. Eigner, P. E. Konold, and A. M. Massari, "Infrared spectroscopic signatures of phase segregation in P3HT-porphyrin blends," J. Phys. Chem. B **113**, 14549–14554 (2009).
[65]B. T. O'Callahan *et al.*, "Imaging nanoscale heterogeneity in ultrathin biomimetic and biological crystals," J. Phys. Chem. C **122**, 24891–24895 (2018).
[66]S. S. Andrews and S. G. Boxer, "Vibrational stark effects of nitriles I. Methods and experimental results," J. Phys. Chem. A **104**, 11853–11863 (2000).
[67]S. Casalini, C. A. Bortolotti, F. Leonardi, and F. Biscarini, "Self-assembled monolayers in organic electronics," Chem. Soc. Rev. **46**, 40–71 (2017).
[68]A. Butterworth *et al.*, "SAM composition and electrode roughness affect performance of a DNA biosensor for antibiotic resistance," Biosensors **9**, 22 (2019).
[69]J. U. Nielsen, M. J. Esplandiu, and D. M. Kolb, "4-nitrothiophenol SAM on Au (111) investigated by in situ STM, electrochemistry, and XPS," Langmuir **17**, 3454–3459 (2001).
[70]F. Liu, Y. Gu, J. W. Jung, W. H. Jo, and T. P. Russell, "On the morphology of polymer-based photovoltaics," J. Polym. Sci., Part B **50**, 1018–1044 (2012).
[71]H. N. Tsao and K. Müllen, "Improving polymer transistor performance via morphology control," Chem. Soc. Rev. **39**, 2372–2386 (2010).
[72]C. R. McNeill, "Morphology of all-polymer solar cells," Energy Environ. Sci. **5**, 5653–5667 (2012).
[73]E. Dhanumalayan and G. M. Joshi, "Performance properties and applications of polytetrafluoroethylene (PTFE)—A review," Adv. Compos. Hybrid Mater. **1**, 247–268 (2018).
[74]G. J. Puts, P. Crouse, and B. M. Ameduri, "Polytetrafluoroethylene: Synthesis and characterization of the original extreme polymer," Chem. Rev. **119**, 1763–1805 (2019).
[75]J. Berg, J. Tymoczko, and L. Stryer, *Biochemistry*, 5th ed. (NCBI, New York, 2002).
[76]J. Shen, B.-I. Noh, P. Chen, and S. Dai, "Scanning probe nano-infrared imaging and spectroscopy of biochemical and natural materials," Small Sci. **4**, 2400297 (2024).
[77]S. Berweger *et al.*, "Nano-chemical infrared imaging of membrane proteins in lipid bilayers," J. Am. Chem. Soc. **135**, 18292–18295 (2013).
[78]D. Abramavicius, W. Zhuang, and S. Mukamel, "Peptide secondary structure determination by three-pulse coherent vibrational spectroscopies: A simulation study," J. Phys. Chem. B **108**, 18034–18045 (2004).
[79]J. Dubochet *et al.*, "Cryo-electron microscopy of vitrified specimens," Q. Rev. Biophys. **21**, 129–228 (1988).
[80]U. B. Gawas, V. K. Mandrekar, and M. S. Majik, "Structural analysis of proteins using x-ray diffraction technique," in *Advances in Biological Science Research* (Elsevier, 2019), pp. 69–84.
[81]C. Bamford, L. Brown, A. Elliott, W. Hanby, and I. Trotter, "Structure of synthetic polypeptides," Nature **169**, 357–358 (1952).
[82]T. Miyazawa, "Perturbation treatment of the characteristic vibrations of polypeptide chains in various configurations," J. Chem. Phys. **32**, 1647–1652 (1960).
[83]A. Barth and C. Zscherp, "What vibrations tell about proteins," Q. Rev. Biophys. **35**, 369–430 (2002).
[84]A. T. Krummel and M. T. Zanni, "DNA vibrational coupling revealed with two-dimensional infrared spectroscopy: Insight into why vibrational spectroscopy is sensitive to DNA structure," J. Phys. Chem. B **110**, 13991–14000 (2006).
[85]N. Qin *et al.*, "Nanoscale probing of electron-regulated structural transitions in silk proteins by near-field IR imaging and nano-spectroscopy," Nat. Commun. **7**, 13079 (2016).
[86]I. Amenabar *et al.*, "Structural analysis and mapping of individual protein complexes by infrared nanospectroscopy," Nat. Commun. **4**, 2890 (2013).
[87]B. T. O'Callahan *et al.*, "In liquid infrared scattering scanning near-field optical microscopy for chemical and biological nanoimaging," Nano Lett. **20**, 4497–4504 (2020).
[88]D. Virmani *et al.*, "Amplitude-and phase-resolved infrared nanoimaging and nanospectroscopy of polaritons in a liquid environment," Nano Lett. **21**, 1360–1367 (2021).
[89]M. Wagner *et al.*, "Ultrafast and nanoscale plasmonic phenomena in exfoliated graphene revealed by infrared pump–probe nanoscopy," Nano Lett. **14**, 894–900 (2014).
[90]M. Eisele *et al.*, "Ultrafast multi-terahertz nano-spectroscopy with sub-cycle temporal resolution," Nat. Photonics **8**, 841–845 (2014).
[91]K. Frischwasser *et al.*, "Real-time sub-wavelength imaging of surface waves with nonlinear near-field optical microscopy," Nat. Photonics **15**, 442–448 (2021).
[92]C. Quarti, A. Milani, and C. Castiglioni, "Ab initio calculation of the IR spectrum of PTFE: Helical symmetry and defects," J. Phys. Chem. B **117**, 706–718 (2013).
[93]A. Bradshaw and F. Hoffmann, "The chemisorption of carbon monoxide on palladium single crystal surfaces: IR spectroscopic evidence for localised site adsorption," Surf. Sci. **72**, 513–535 (1978).
[94]S. Berweger *et al.*, "Optical nanocrystallography with tip-enhanced phonon Raman spectroscopy," Nat. Nanotechnol. **4**, 496–499 (2009).
[95]H. U. Yang, E. Hebestreit, E. E. Josberger, and M. B. Raschke, "A cryogenic scattering-type scanning near-field optical microscope," Rev. Sci. Instrum. **84**, 023701 (2013).
[96]R. H. Kim, J.-M. Park, S. J. Haeuser, L. Luo, and J. Wang, "A sub-2 Kelvin cryogenic magneto-terahertz scattering-type scanning near-field optical microscope (cm-THz-sSNOM)," Rev. Sci. Instrum. **94**, 043702 (2023).
[97]K.-T. Lin, Q. Weng, S. Kim, S. Komiyama, and Y. Kajihara, "Development of a cryogenic passive-scattering-type near-field optical microscopy system," Rev. Sci. Instrum. **94**, 023701 (2023).